The Astrophysical Journal Letters, 993:L20 (14pp), 2025 November 1 https://doi.org/10.3847/2041-8213/ae0e70

Masses, Star Formation Efficiencies, and Dynamical Evolution of 18,000 H II Regions

Debosmita Pathak[1,2], Adam K. Leroy[1,2], Ashley. T. Barnes[3], Todd A. Thompson[1,2,4], Laura A. Lopez[1,2], Karin M. Sandstrom[5], Jiayi Sun[6,7,39], Simon C. O. Glover[8], Ralf S. Klessen[8,9], Eric W. Koch[10,11], Kirsten L. Larson[12], Janice Lee[12], Sharon Meidt[13], Patricia Sanchez-Blazquez[14], Eva Schinnerer[15], Zein Bazzi[16], Francesco Belfiore[17], Médéric Boquien[18], Ryan Chown[1], Dario Colombo[16], Enrico Congiu[19], Oleg V. Egorov[20], Cosima Eibensteiner[21,40], Sushma Kurapati[22], Miguel Querejeta[23], Daniel A. Dale[24], Timo Kravtsov[25], Mansi Padave[5], D. J. Pisano[26], Erik Rosolowsky[27], Sumit K. Sarbadhicary[28,29,30], Thomas G. Williams[31], Remy Indebetouw[32], Hsi-An Pan[33], Leonardo Úbeda[34], Amirnezam Amiri[35], Frank Bigiel[16], Guillermo A. Blanc[36,37], and Kathryn Grasha[38]

[1] Department of Astronomy, Ohio State University, 180 West 18th Avenue, Columbus, OH 43210, USA; pathak.89@buckeyemail.osu.edu
[2] Center for Cosmology and Astroparticle Physics, 191 West Woodruff Avenue, Columbus, OH 43210, USA
[3] European Southern Observatory, Karl-Schwarzschild-Straße 2, 85748 Garching, Germany
[4] Department of Physics, Ohio State University, 91 West Woodruff Avenue, Columbus, OH 43210, USA
[5] Department of Astronomy & Astrophysics, University of California, San Diego, 9500 Gilman Drive, La Jolla, CA 92093, USA
[6] Department of Astrophysical Sciences, Princeton University, 4 Ivy Lane, Princeton, NJ 08544, USA
[7] Department of Physics and Astronomy, University of Kentucky, 505 Rose Street, Lexington, KY 40506, USA
[8] Universität Heidelberg, Zentrum für Astronomie, Institut für Theoretische Astrophysik, Albert-Ueberle-Str. 2, 69120 Heidelberg, Germany
[9] Universität Heidelberg, Interdisziplinäres Zentrum für Wissenschaftliches Rechnen, Im Neuenheimer Feld 225, 69120 Heidelberg, Germany
[10] National Radio Astronomy Observatory, 800 Bradbury SE, Suite 235, Albuquerque, NM 87106, USA
[11] Center for Astrophysics — Harvard & Smithsonian, 60 Garden Street, Cambridge, MA 02138, USA
[12] AURA for the European Space Agency (ESA), Space Telescope Science Institute, 3700 San Martin Drive, Baltimore, MD 21218, USA
[13] Sterrenkundig Observatorium, Universiteit Gent, Krijgslaan 281 S9, B-9000 Gent, Belgium
[14] Facultad de CC Físicas & IPARCOS, Universidad Complutense de Madrid, Plaza de las Ciencias 1, 28040, Madrid, Spain
[15] Max-Planck-Institut für Astronomie, Königstuhl 17, D-69117 Heidelberg, Germany
[16] Argelander-Institut für Astronomie, University of Bonn, Auf dem Hügel 71, 53121 Bonn, Germany
[17] INAF—Osservatorio Astrofisico di Arcetri, Largo E. Fermi 5, I-50157, Firenze, Italy
[18] Université Côte d'Azur, Observatoire de la Côte d'Azur, CNRS, Laboratoire Lagrange, 06000, Nice, France
[19] European Southern Observatory (ESO), Alonso de Córdova 3107, Casilla 19, Santiago 19001, Chile
[20] Astronomisches Rechen-Institut, Zentrum für Astronomie der Universität Heidelberg, Mönchhofstraße 12-14, D-69120 Heidelberg, Germany
[21] National Radio Astronomy Observatory, 520 Edgemont Road, Charlottesville, VA 22903, USA
[22] Netherlands Institute for Radio Astronomy (ASTRON), Oude Hoogeveensedijk 4, 7991 PD Dwingeloo, The Netherlands
[23] Observatorio Astronómico Nacional (IGN), C/Alfonso XII 3, Madrid E-28014, Spain
[24] Department of Physics and Astronomy, University of Wyoming, Laramie, WY 82071, USA
[25] Department of Physics and Astronomy, University of Turku, 20014 Turku, Finland
[26] University of Cape Town, Private Bag X3, Rondebosch, 7701, Republic of South Africa
[27] Department of Physics, University of Alberta, 4-183 CCIS, Edmonton, AB T6G 2E1, Canada
[28] Department of Physics and Astronomy, The Johns Hopkins University, Baltimore, MD 21218, USA
[29] Department of Physics, The Ohio State University, Columbus, OH 43210, USA
[30] Center for Cosmology & Astro-Particle Physics, The Ohio State University, Columbus, OH 43210, USA
[31] Sub-department of Astrophysics, Department of Physics, University of Oxford, Keble Road, Oxford OX1 3RH, UK
[32] Astronomy Deptartment, University of Virginia, P.O. Box 400325, Charlottesville, VA 22904, USA
[33] Department of Physics, Tamkang University, No.151, Yingzhuan Road, Tamsui District, New Taipei City 251301, Taiwan
[34] Space Telescope Science Institute, Baltimore, MD 21218, USA
[35] Department of Physics, University of Arkansas, 226 Physics Building, 825 West Dickson Street, Fayetteville, AR 72701, USA
[36] Observatories of the Carnegie Institution for Science, 813 Santa Barbara Street, Pasadena, CA 91101, USA
[37] Departamento de Astronomía, Universidad de Chile, Camino del Observatorio 1515, Las Condes, Santiago, Chile
[38] Research School of Astronomy and Astrophysics, Australian National University, Canberra, ACT 2611, Australia
Received 2025 July 31; revised 2025 September 25; accepted 2025 September 26; published 2025 October 24

Abstract

We present measurements of the masses associated with ∼18,000 H II regions across 19 nearby star-forming galaxies by combining data from JWST, Hubble Space Telescope, MUSE, Atacama Large Millimeter/submillimeter Array, Very Large Array, and MeerKAT from the multiwavelength PHANGS survey. We report 10 pc-scale measurements of the mass of young stars, ionized gas, and older disk stars coincident with each H II region, as well as the initial and current mass of molecular gas, atomic gas, and swept-up shell material, estimated from lower-resolution data. We find that the mass of older stars dominates over young stars at $\gtrsim$10 pc scales, and ionized gas exceeds the stellar mass in most optically bright H II regions. Combining our mass measurements for a

[39] NASA Hubble Fellow.
[40] Jansky Fellow of the National Radio Astronomy Observatory.

statistically large sample of H II regions, we derive 10 pc-scale star formation efficiencies of ≈6%–17% for individual H II regions. Comparing each region's self-gravity with the ambient interstellar medium (ISM) pressure and total pressure from presupernova stellar feedback, we show that most optically bright H II regions are overpressured relative to their own self-gravity and the ambient ISM pressure and that they are hence likely expanding into their surroundings. Larger H II regions in galaxy centers approach dynamical equilibrium. The self-gravity of regions is expected to dominate over presupernova stellar feedback pressure at $\gtrsim$130 and 60 pc scales in galaxy disks and centers, respectively, but is always subdominant to the ambient ISM pressure on H II region scales. Our measurements have direct implications for the dynamical evolution of star-forming regions and the efficiency of stellar feedback in ionizing and clearing cold gas.

Unified Astronomy Thesaurus concepts: Stellar feedback (1602); H II regions (694); Interstellar medium (847); Extragalactic astronomy (506); Star formation (1569); Star forming regions (1565)

Materials only available in the online version of record: machine-readable table

1. Introduction

H II regions trace the sites of recent massive star formation, created when young, massive OB stars ionize their surroundings. They have typical sizes of $\lesssim$100 pc and can be easily identified by their strong nebular line (Hα) and IR dust emission (e.g., R. C. Kennicutt & N. J. Evans 2012). Within H II regions, young, massive stars exert multiple modes of feedback on the surrounding interstellar medium (ISM), including warm gas pressure, radiation pressure, stellar winds, and supernova feedback. As a result, H II regions are key laboratories for studying star formation, stellar feedback, chemical enrichment, and dynamical evolution in the ISM (e.g., E. Schinnerer & A. K. Leroy 2024).

Recent high physical resolution (∼10–50 pc) multiwavelength observations have made it possible to build a comprehensive view of large samples of H II regions beyond the Local Group (e.g., A. T. Barnes et al. 2021, 2022; S. Hannon et al. 2022; F. Scheuermann et al. 2022; A. Pedrini et al. 2024; D. Pathak et al. 2025) including ∼18,000 regions with a detailed characterization of the stellar feedback properties (D. Pathak et al. 2025). These build on previous detailed studies of H II regions in the Milky Way (e.g., A. T. Barnes et al. 2020; G. M. Olivier et al. 2021), Magellanic Clouds (e.g., L. A. Lopez et al. 2011, 2014), and local galaxies (<5 Mpc; e.g., R. C. Levy et al. 2021; A. F. McLeod et al. 2021; M. Cosens et al. 2022; L. Della Bruna et al. 2022).

While feedback in H II regions has been extensively studied, the masses of these star-forming regions have received comparatively less attention. A careful accounting of the mass of ionized, molecular, and atomic gas, as well as young and old stars, is necessary to understand the impact of stellar feedback on the dynamical evolution of H II regions and to estimate star formation efficiencies (SFEs), i.e., the fraction of gas converted to stars. This Letter presents the first comprehensive inventory of the masses associated with a statistically large sample of H II regions across nearby galaxies, with corresponding estimates of the SFE and dynamical state (see, e.g., E. Churchwell & W. M. Goss 1999; M. Relaño et al. 2005; M. Cosens et al. 2022 for case studies with smaller samples).

For ∼18,000 H II regions across 19 nearby galaxies, we present new 10 pc-scale measurements of the mass of

1. young stars (Section 2.1.1),
2. ionized gas (Section 2.1.2),
3. older stars from the galactic disk (Section 2.1.3),
4. initial molecular gas (Section 2.2.1), and
5. additional disk components (initial atomic gas and bounds on dark matter and hot X-ray-emitting gas mass; Section 2.2.2).

We discuss the implications of our estimates for the efficiency of stellar feedback in ionizing and clearing local gas (Section 3.2) and the dynamical state of H II regions (Section 3.3). The analyzed H II regions account for the bulk of ongoing star formation in our galaxy sample (e.g., F. Belfiore et al. 2022; E. Emsellem et al. 2022). Therefore, we expect their properties to be representative of H II regions in normal star-forming galaxies in the $z \approx 0$ Universe.

2. Estimating Mass Associated with H II Regions

We estimate the masses associated with ∼18,000 H II regions (Figure 1, Table 1) across 19 nearby spiral galaxies that have been observed by the Physics at High Angular resolution in Nearby GalaxieS (PHANGS) surveys (A. K. Leroy et al. 2021; E. Emsellem et al. 2022; J. C. Lee et al. 2023), including coverage by Hα imaging with 10 pc physical resolution (A. T. Barnes et al. 2025; R. Chandar et al. 2025). The sample spans the star-forming main sequence, including 17 barred galaxies and two lower-mass spirals (A. K. Leroy et al. 2021; E. Emsellem et al. 2022; J. C. Lee et al. 2023; T. G. Williams et al. 2024). Our H II regions are drawn from the PHANGS-MUSE nebular catalog (B. Groves et al. 2023; see also K. Kreckel et al. 2019; F. Santoro et al. 2022), which includes 17,615 Baldwin–Phillips–Terlevich-selected H II regions with joint MUSE, JWST, Hubble Space Telescope (HST), and Atacama Large Millimeter/submillimeter Array (ALMA) coverage (same as D. Pathak et al. 2025).

2.1. Current Masses

2.1.1. Young Stars

The mass of the young stars powering each region, $M_{\rm New}$, is estimated from its extinction-corrected Hα luminosity, $L_{\rm H\alpha}^{\rm corr}$ (A. T. Barnes et al. 2025; R. Chandar et al. 2025; for details see D. Pathak et al. 2025). As in D. Pathak et al. (2025), we use HST narrowband Hα luminosities where available and translate MUSE luminosities to be consistent with HST sizes otherwise (see Appendix A in D. Pathak et al. 2025 for details). Extinctions are estimated from MUSE Balmer decrements (E. Emsellem et al. 2022; F. Belfiore et al. 2023; B. Groves et al. 2023).

To translate the observed $L_{\rm H\alpha}^{\rm corr}$ to an associated young stellar mass, we calculate the bolometric luminosity-weighted average H-ionizing luminosity over the first 4 Myr (before the ionizing photon flux drops and supernovae go off; see

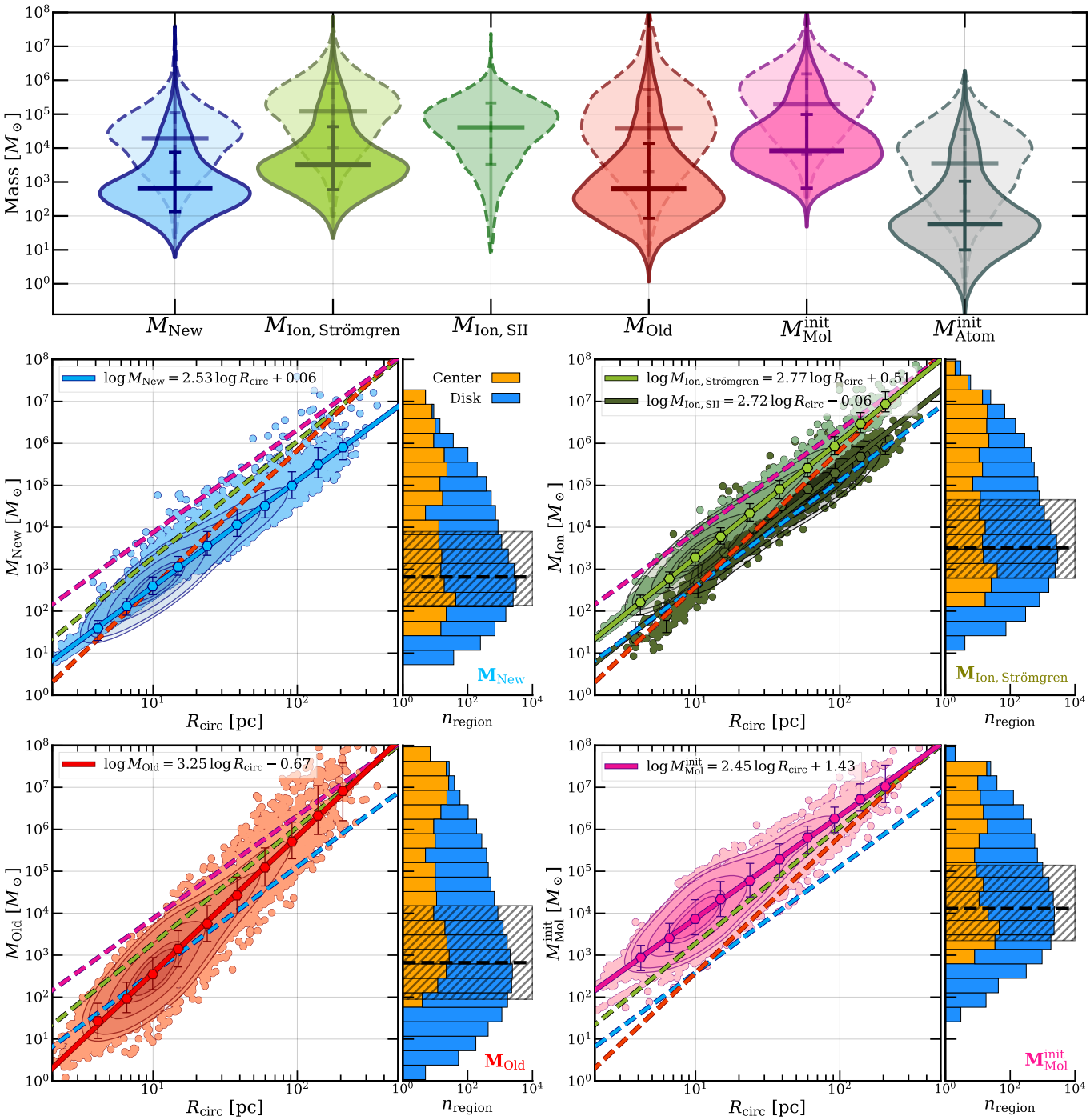

Figure 1. The distribution of masses associated with our sample of ∼18,000 H II regions (solid violins) and the subsample of ∼4000 regions where we can calculate [S II] densities (dashed violins), including contributions from young clusters ($M_{\rm New}$, in blue; see Section 2.1.1), ionized gas mass ($M_{\rm Ion}$, Strömgren in light green and [S II]-emitting clump in dark green; see Section 2.1.2), old stellar mass ($M_{\rm Old}$, in red; see Section 2.1.3), initial molecular gas mass ($M^{\rm init}_{\rm Mol}$, in pink; Section 2.2.1), and initial atomic gas mass ($M^{\rm init}_{\rm Atom}$, in gray; Section 2.2.2) as violin plots with the median and 16th–84th range included. Below we show how $M_{\rm New}$, $M_{\rm Ion}$, $M_{\rm Old}$, and $M^{\rm init}_{\rm Mol}$ scale with physical size ($R_{\rm circ}$). Contours show the 16th/25th/50th/75th/84th percentiles, and we include log–log fits (bold lines, repeated as dashed lines in each panel) to the binned medians (hexagons) and the 16th–84th percentile scatter in each bin (error bars on hexagons). Attached to each scatter plot are stacked histograms of region masses for galaxy centers (orange) and disks (blue) (following M. Querejeta et al. 2021), the sample median (dashed line), and the 16th–84th percentile range (hatches).

A. T. Barnes et al. 2021) of simple stellar population (SSP) evolution with the default STARBURST99 (C. Leitherer et al. 1999, 2014) parameters,[41] which we then compare to the ionizing luminosity of each region (consistent with A. T. Barnes et al. 2021; D. Pathak et al. 2025). This yields $M_{\rm New}/L_{\rm H\alpha}{}^{\rm SB\ 99} = 0.112\,M_\odot/L_\odot$.[42]

[41] Run for a $10^6\,M_\odot$ cluster with a fully populated P. Kroupa (2001) IMF with a maximum stellar mass of $100\,M_\odot$, at solar metallicity, and for nonrotating stars.

[42] For a fully sampled IMF, the conversion from $L_{\rm H\alpha}$ to $M_{\rm New}$ depends on the age of the stellar population, with commonly used values of $M_{\rm New}/L_{\rm H\alpha}{}^{\rm SB\ 99}$ ranging from ≈0.08 to 0.18 $M_\odot/L_\odot$ (see discussion in D. Pathak et al. 2025).

Table 1
Masses, Mass Ratios, SFEs, and H II Region Pressures

Quantity	Formula	Unit	Median
Masses (Section 2)			
Young stars (Section 2.1.1)	$M_{\rm New} = \frac{0.112\,M_\odot}{L_\odot} \times \frac{L_{\rm H\alpha}{}^{\rm corr}}{(1-f_{\rm esc})}$	$\log M_\odot$	$2.81^{3.88}_{2.12}$
Strömgren ionized gas (Section 2.1.2)	$M_{\rm Ion,\,Strömgren} = 1.36\,m_{\rm H}\,n_{\rm H,\,Strömgren}\frac{4}{3}\pi R_{\rm circ}^3$	$\log M_\odot$	$3.5^{4.63}_{2.78}$
[a][S II] ionized gas (Section 2.1.2)	$M_{\rm Ion,\,S\,II} = 1.36\,m_{\rm H}\,\frac{L_{\rm H\alpha}{}^{\rm corr}}{0.45\,\langle h\nu\rangle_{\rm H\alpha}\,\alpha_{\rm B}\,n_{\rm e,S\,II}}$	$\log M_\odot$	$4.61^{5.33}_{3.51}$
Older disk stars (Section 2.1.3)	$M_{\rm Old} = \frac{\Sigma_{\rm Old}}{2h_z^{\rm exp}}\frac{4}{3}\pi R_{\rm circ}^3$	$\log M_\odot$	$2.8^{4.14}_{1.93}$
Total enclosed mass	$M_{\rm Enclosed} = M_{\rm New} + M_{\rm Ion,\,Strömgren} + M_{\rm Old}$	$\log M_\odot$	$3.67^{4.83}_{2.93}$
Initial molecular gas (Section 2.2.1)	$M_{\rm Mol}^{\rm init} = \langle\Sigma_{\rm Mol}\rangle_{150}\,\pi R_{\rm circ}^2$	$\log M_\odot$	$4.1^{5.12}_{3.33}$
Initial atomic gas (Section 2.2.2)	$M_{\rm Atom}^{\rm init} = 1.36\,m_{\rm H\,I}\frac{N({\rm H\,I})}{h_{\rm H\,I}^{\rm FWHM}}\frac{4}{3}\pi R_{\rm circ}^3$	$\log M_\odot$	$1.83^{3.1}_{0.98}$
Mass Ratios (Section 3.1)			
Young stars versus Strömgren ionized gas	$\frac{M_{\rm Ion,\,Strömgren}}{M_{\rm New}}$	⋯	$5.01^{6.48}_{3.99}$
[a]Young stars versus [S II] ionized gas	$\frac{M_{\rm Ion,\,S\,II}}{M_{\rm New}}$	⋯	$1.89^{3.13}_{1.0}$
Young stars versus older stars	$\frac{M_{\rm Old}}{M_{\rm New}}$	⋯	$1.01^{3.1}_{0.41}$
Current versus initial mass	$\frac{M_{\rm New}+M_{\rm Ion,\,Strömgren}}{M_{\rm Mol}^{\rm init}+M_{\rm Atom}^{\rm init}}$	⋯	$0.33^{0.73}_{0.15}$
Current mass versus molecular gas depletion	$\frac{M_{\rm New}+M_{\rm Ion,\,Strömgren}}{M_{\rm Mol}^{\rm init}-M_{\rm Mol}^{\rm current}}$	⋯	$0.55^{2.15}_{0.19}$
150 pc molecular gas depletion	$\frac{M_{\rm Mol}^{\rm init}-M_{\rm Mol}^{\rm current}}{M_{\rm Mol}^{\rm init}}$	⋯	$0.38^{0.8}_{-0.43}$
Star Formation Efficiencies (Section 3.2)			
Frac. of current enclosed mass in stars (Strömgren)	$\epsilon = \frac{M_{\rm New}}{M_{\rm New}+M_{\rm Ion,\,Strömgren}}$	⋯	$0.17^{0.2}_{0.13}$
[a]Frac. of current enclosed mass in stars ([S II])	$\epsilon = \frac{M_{\rm New}}{M_{\rm New}+M_{\rm Ion,\,S\,II}}$	⋯	$0.35^{0.5}_{0.24}$
Frac. of total current mass in stars (Strömgren)	$\epsilon = \frac{M_{\rm New}}{M_{\rm New}+M_{\rm Ion,\,Strömgren}+M_{\rm Mol}^{\rm current}}$	⋯	$0.06^{0.1}_{0.04}$
[a]Frac. of total current mass in stars ([S II])	$\epsilon = \frac{M_{\rm New}}{M_{\rm New}+M_{\rm Ion,\,S\,II}+M_{\rm Mol}^{\rm current}}$	⋯	$0.08^{0.14}_{0.05}$
Frac. of initial molecular mass in stars	$\epsilon = \frac{M_{\rm New}}{M_{\rm Mol}^{\rm init}}$	⋯	$0.06^{0.13}_{0.03}$
Frac. of depleted molecular mass in stars	$\epsilon = \frac{M_{\rm New}}{M_{\rm Mol}^{\rm init}-M_{\rm Mol}^{\rm current}}$	⋯	$0.09^{0.34}_{0.03}$
Pressures (Section 3.3)			
Region self-gravity	$P_{\rm Grav} = \frac{GM_{\rm sh}(M_{\rm Enclosed}+\frac{1}{2}M_{\rm sh})}{4\pi R_{\rm circ}^4}$	$\log {\rm K\,cm^{-3}}$	$3.59^{4.39}_{3.03}$
Presupernova feedback	$P_{\rm Feedback} = P_{\rm Therm} + P_{\rm Rad} + P_{\rm Wind} + P_{\rm X}$	$\log {\rm K\,cm^{-3}}$	$5.49^{5.6}_{5.41}$
Overpressure	$\frac{P_{\rm Feedback}}{P_{\rm Grav}+\langle P_{\rm DE}\rangle}$	⋯	$2.66^{8.8}_{0.52}$

Notes. Summarizing key definitions, units, and main results (as median$^{\rm 84th\ percentile}_{\rm 16th\ percentile}$) for masses, mass ratios, SFEs, and pressures of 18,000 H II regions. See Table 2 for a more detailed summary and Table 3 for the full data set.
[a] From [S II] doublet $n_{\rm e,\,S\,II}$ for a subset of 3221 H II regions (Section 2.1.2).

We correct the observed $L_{\rm H\alpha}{}^{\rm corr}$ to take into account the fraction of ionizing photons escaping the region, $f_{\rm esc}$, as $L_{\rm H\alpha}{}^{\rm corr}/(1-f_{\rm esc})$. Theory predicts large variations in $f_{\rm esc}$ due to environment and geometry (e.g., C. S. Howard et al. 2018; J.-G. Kim et al. 2019; C.-C. He et al. 2020; T. Kimm et al. 2022; S. H. Menon et al. 2025). While mean $f_{\rm esc}\sim30\%\pm10\%$ for H II regions in normal star-forming galaxies, $f_{\rm esc}$ for any individual region is highly uncertain (e.g., F. Belfiore et al. 2022; F. Scheuermann et al. 2022; A. T. Barnes et al. 2025). We thus assume a fixed $f_{\rm esc}=0.3$ and estimate $M_{\rm New}$ as

$$M_{\rm New} = \frac{0.112\,M_\odot}{L_\odot}\times\frac{L_{\rm H\alpha}{}^{\rm corr}}{(1-f_{\rm esc})} = 160\left(\frac{L_{\rm H\alpha}{}^{\rm corr}}{10^3\,L_\odot}\right)\left(\frac{1-f_{\rm esc}}{0.7}\right)^{-1}M_\odot. \quad (1)$$

Note that Equation (1) does not account for the $E>24.5$ eV photons absorbed by helium (∼5%–10% level effect) or ionizing photons that are absorbed by dust before H ionization,

which leads to a likely underestimate of the total mass of young stars. Absorption by dust can be significant, especially in the massive and dusty H II regions in galaxy centers (∼30%, see B. A. Binder & M. S. Povich 2018; or ∼10%–50%, see J.-G. Kim et al. 2019; S. H. Menon et al. 2025). However, most regions in our sample show relatively low $A_V \approx 0.6$–1 mag (see D. Pathak et al. 2025), where this fraction is expected to be much lower but remains unconstrained.

We likely underestimate $M_{\rm New}$ for most clusters at low ${L_{\rm H\alpha}}^{\rm corr}$, since our conversion is based on SSP models that are nonstochastic (see, e.g., R. L. da Silva et al. 2012 for stochastic initial mass function, IMF, sampling) and do not include binaries (e.g., Y. Götberg et al. 2020). Binaries may cause additional ionization at ages $\gtrsim$10 Myr. It is uncertain to what degree these populations affect H II regions, but both topics are expected to be the subject of follow-up work in PHANGS.

2.1.2. Ionized Gas

The ionized gas mass can be determined from the Hα luminosity assuming Case B recombination with a given volume density. We estimate the ionized gas density in two ways: (1) using the Strömgren sphere approximation and (2) from the [S II] doublet ratio. These yield upper and lower bounds on the total ionized gas mass, respectively.

For a smooth spherical gas distribution (clumping factor $f_c = 1$) with a fixed density, the Strömgren calculation yields

$$n_{\rm H,\ Strömgren} = \sqrt{\frac{3Q_0}{4\pi\alpha_B R_{\rm circ}^3 f_e f_c}}, \tag{2}$$

where $1.367Q_0/{\rm s}^{-1} = 10^{12}{L_{\rm H\alpha}}^{\rm corr}/({\rm erg\ s}^{-1})$ (D. E. Osterbrock & G. J. Ferland 2006) and the factor of $f_e = 1.08$ accounts for electrons from singly ionized He in addition to H at an abundance representative of the ISM of external galaxies (as in A. D. Bolatto et al. 2013), assuming $M_{\rm He} + M_{\rm H} = 1.36\,M_{\rm H}$ or $n_{\rm He}/n_{\rm H} = 0.08$. $\alpha_B = 3.1 \times 10^{-13}\,{\rm cm^3\,s^{-1}}$ is the Case B H-recombination coefficient at electron temperature $T_e = 8000$ K (P. J. Storey & D. G. Hummer 1995) representative of the PHANGS-MUSE sample (O. V. Egorov et al. 2023). $R_{\rm circ}$ is the circularized radius corresponding to an isophotal area measured from 10 pc-resolution HST narrow-band Hα imaging (see A. T. Barnes et al. 2025). The corresponding H II and ionized gas mass of an H II region is then

$$\begin{aligned} M_{\rm H\,II,\ Strömgren} &= m_{\rm H}\, n_{\rm H,\ Strömgren} \frac{4}{3}\pi R_{\rm circ}^3, \\ M_{\rm Ion,\ Strömgren} &= 1.36\, M_{\rm H\,II,\ Strömgren} \\ &= 1.2 \times 10^3 \left(\frac{{L_{\rm H\alpha}}^{\rm corr}}{10^3\,L_\odot}\right)^{1/2} \left(\frac{R_{\rm circ}}{10\ {\rm pc}}\right)^{3/2} M_\odot. \end{aligned} \tag{3}$$

Two caveats are worth bearing in mind. First, there is some ambiguity regarding the appropriate size. We use $R_{\rm circ}$, based on the area above a fixed Hα intensity threshold in the HST maps, which matches the region used to derive cluster and gas properties. However, this threshold captures varying fractions of the total Hα flux—e.g., going down in sensitivity to ∼10% of the peak value in bright regions (and therefore a large fraction of the total flux) as compared to only down to ∼50% in faint H II regions (and therefore a smaller fraction of the total flux) Second, Equation (2) assumes a uniform volume density ($f_c = 1$), while the actual ionized gas distribution is generally more clumpy ($f_c > 1$; see, e.g., L. Lancaster et al. 2025). As a result, the Strömgren estimate represents a *lower* bound on the actual physical density $n_{\rm H}$ of the clumpy Hα-emitting gas but an *upper* bound on the volume-averaged ionized gas density $\langle n_{\rm H}\rangle$ and hence an upper bound on the total ionized gas mass.

We also use the [S II] line ratio to estimate the electron number density $n_{\rm e,\ S\,II}$ using PYNEB (V. Luridiana et al. 2015) for a subset of 3221 regions where the [S II] ratio differs from the low-density limit at high confidence (see also A. T. Barnes et al. 2021, 2025). Assuming that the Hα emission comes from the same volume probed by the [S II] doublet ($V_{\rm S\,II}$), we balance the observed Hα luminosity against the recombination rate (D. E. Osterbrock & G. J. Ferland 2006) suggested by $n_{\rm e,\ S\,II}$:

$$\begin{aligned} {L_{\rm H\alpha}}^{\rm corr} &= 0.45\,\langle h\nu\rangle_{\rm H\alpha}\, n_e\, n_{\rm H}\, \alpha_B\, V_{\rm S\,II} \\ &= 0.45\,\langle h\nu\rangle_{\rm H\alpha} \frac{n_{\rm e,\ S\,II}^2}{f_e} \alpha_B\, V_{\rm S\,II}. \end{aligned} \tag{4}$$

Then,

$$\begin{aligned} M_{\rm H\,II,\ S\,II} &= m_{\rm H} \frac{n_{\rm e,\ S\,II}}{f_e} V_{\rm S\,II}, \\ M_{\rm Ion,\ S\,II} &= 1.36\, M_{\rm H\,II,\ S\,II} \\ &= 2.1 \times 10^2 \left(\frac{{L_{\rm H\alpha}}^{\rm corr}}{10^3\,L_\odot}\right) \left(\frac{n_{\rm e,\ S\,II}}{50\ {\rm cm^{-3}}}\right)^{-1} M_\odot. \end{aligned} \tag{5}$$

Since [S II] emission increases with density, $n_{\rm e,\ S\,II}$ traces the densest clumps of ionized gas. We expect this to represent an upper limit to the physical density and a lower limit to the total mass (see O. V. Egorov et al. 2023 for details of using MUSE density diagnostics). Finally, the [S II] doublet enters the low-density limit for many of our regions (see A. T. Barnes et al. 2021), biasing the sample where $n_{\rm e,\ S\,II}$ estimates are possible toward the densest regions.

2.1.3. Older Stars in the Galactic Disk

The H II regions in nearby disk galaxies evolve within a massive, extended galactic disk of older (≫10 Myr) stars that contribute to the mass enclosed within the H II region. We estimate this contribution using inclination-corrected JWST/NIRCam F300M (3 μm) intensities (J. C. Lee et al. 2023; for details on data processing, see T. G. Williams et al. 2024).

We calculate the F300M surface brightness profile of the galaxies and evaluate its value $I_{3\,\mu\rm m}$ at the galactic radius of each region to estimate the stellar mass surface density of disk stars, $\Sigma_{\rm Old}$, via

$$\frac{\Sigma_{\rm Old}}{M_\odot\ {\rm pc^{-2}}} = 2.6 \times 10^2 \left(\frac{\Upsilon_*}{0.5}\right) \left(\frac{I_{3\,\mu\rm m}}{1\ {\rm MJy\ sr^{-1}}}\right), \tag{6}$$

where Υ_* is the mass-to-light ratio in solar units. We adopt the specific star-formation-rate-dependent near-IR Υ_* from A. K. Leroy et al. (2019), implemented in J. Sun et al. (2022) (see those papers for more details), which shows good consistency with MUSE stellar mass surface densities (E. Emsellem et al. 2022). Compared to A. K. Leroy et al. (2019), which utilized 3.4 μm emission, we adjust the

prefactor in Equation (6) assuming that the Sun's spectrum follows a Rayleigh–Jeans distribution $L_\nu \propto \nu^2$ near 3 μm. Here we use the radial profile rather than evaluating $I_3\,\mu$m at the location of the region to avoid contamination of this estimate by the young stellar population. S. E. Meidt et al. (2021) and M. Querejeta et al. (2024) show that azimuthal variations in stellar structure are relatively modest ($\lesssim$20%–30%) in these targets.

Assuming a vertical scale height of the stellar disk $h_z^{\rm exp} = L_*/7.3$ (for an exponential vertical density profile, as in M. Kregel et al. 2002),[43] where L_* is the exponential scale length of the disk, we derive the average background stellar mass density,

$$\rho_{\rm Old} = \frac{\Sigma_{\rm Old}}{2h_z^{\rm exp}},$$

$$\frac{\rho_{\rm Old}}{M_\odot\ {\rm pc}^{-3}} = 0.52\left(\frac{\Upsilon_*}{0.5}\right)\left(\frac{I_{3\,\mu{\rm m}}}{1\ {\rm MJy\ sr}^{-1}}\right)\left(\frac{2h_z^{\rm exp}}{500\ {\rm pc}}\right)^{-1}, \quad (7)$$

at the galactocentric radius of each H II region. We record $\rho_{\rm Old}$ in Table 2. Given this density and a volume, with the assumption that H II regions lie close to the midplane (within $2h_z^{\rm exp}$), we can estimate the mass ($M_{\rm Old}$) of disk stars. For our adopted footprint size, $R_{\rm circ}$, we calculate $M_{\rm Old}$ within each region as

$$M_{\rm Old} = \rho_{\rm Old} \times \frac{4}{3}\pi R_{\rm circ}^3. \quad (8)$$

2.2. Initial Gas Masses

2.2.1. Molecular Gas

We also estimate the initial molecular gas mass associated with each H II region before star formation. We use the mass-weighted average molecular gas surface density (using the $\alpha_{\rm CO}$ prescription from E. Schinnerer & A. K. Leroy 2024) at 150 pc resolution, $\langle\Sigma_{\rm Mol}\rangle_{150}$, within the 1.5 kpc diameter hexagonal region containing that region calculated by J. Sun et al. (2022). This provides an estimate of the typical surface density of molecular clouds in the same part of the galaxy as the target region, and we expect that it represents a reasonable estimate of the initial conditions before feedback. We assume the molecular gas scale height to be of the same order as the H II region sizes. Therefore, we estimate the initial molecular gas mass from the area of each H II region footprint,

$$M_{\rm Mol}^{\rm init} = 1.36\ \langle\Sigma_{\rm H_2}\rangle_{150}\ \pi R_{\rm circ}^2 = \langle\Sigma_{\rm Mol}\rangle_{150}\ \pi R_{\rm circ}^2,$$

$$\frac{M_{\rm Mol}^{\rm init}}{M_\odot} = 3.1\times10^3\left(\frac{\langle\Sigma_{\rm Mol}\rangle_{150}}{10\ M_\odot\ {\rm pc}^{-2}}\right)\left(\frac{R_{\rm circ}}{10\ {\rm pc}}\right)^2. \quad (9)$$

Note that the 150 pc resolution used here is larger than the the size of the H II regions. $\langle\Sigma_{\rm Mol}\rangle_{150}$ is predictive of the surface densities at higher resolution (120, 90, and 60 pc), but due to clumping, the higher resolutions show higher $\langle\Sigma_{\rm Mol}\rangle$ (J. Sun et al. 2018, 2022; A. K. Leroy et al. 2025); for example, $\langle\Sigma_{\rm Mol}\rangle_{60}$ is $\approx$0.13 dex or 1.35$\times$ higher than $\langle\Sigma_{\rm Mol}\rangle_{150}$ in A. K. Leroy et al. (2025). Based on this, we might expect our $M_{\rm Mol}$ to be underestimated by $\sim$25%–50%.

Our $M_{\rm Mol}^{\rm init}$ thus represents a statistical estimate of the original mass. We also measure the *current* $\Sigma_{\rm Mol}$ at the location of each region. Although we do not expect that there is significant molecular gas within the H II regions themselves, this measurement captures any molecular gas near the region. Contrasting the current 150 pc associated and estimated initial $\langle\Sigma_{\rm Mol}\rangle_{150}$ also provides a statistical constraint on how much local gas is ionized and cleared by feedback (see Section 3.2).

2.2.2. Additional Disk Components

In addition to stars, galaxy disks contain atomic gas and dark matter. Although we expect H I within the H II region to be dispersed or ionized, we estimate the likely initial atomic gas mass of each region based on lower-resolution 21 cm H I mapping from MeerKAT (IC 5332, NGC 1300, NGC 1512, NGC 1566, NGC 1672, NGC 4535, NGC 5068, and NGC 7496; W. J. G. de Blok et al. 2024; C. Eibensteiner et al. 2024; D. J. Pisano et al. 2025, in preparation) and the Very Large Array (VLA; NGC 0628, NGC 1087, NGC 1385, NGC 3351, NGC 2835, NGC 3627, NGC 4254, NGC 4303, and NGC 4321; F. Walter et al. 2008; A. Chung et al. 2009; I.-D. Chiang et al. 2024). No H I data were available for NGC 1365 and NGC 1433. We estimate the H I column density toward each region at 2 kpc resolution from the inclination-corrected integrated intensity,

$$\frac{N({\rm H\,I})}{{\rm cm}^{-2}} = 1.823\times10^{18}\frac{I_{\rm H\,I}}{{\rm K\ km\ s}^{-1}}, \quad (10)$$

and the corresponding midplane initial atomic gas density assuming the H I is optically thin, $\rho_{\rm Atom} = 1.36\,m_{\rm H\,I}N({\rm H\,I})/h_{\rm H\,I}^{\rm FWHM}$, where $h_{\rm H\,I}^{\rm FWHM}$ is the vertical FWHM of the H I gas disk (generally $h_{\rm H\,I}^{\rm FWHM} > 2h_z^{\rm exp}$). We set $h_{\rm H\,I}^{\rm FWHM} = 1$ kpc, typical for the optical disk of star-forming massive spiral galaxies (see, e.g., T. H. Randriamampandry et al. 2021; Y. Zheng et al. 2022). The initial atomic gas mass $M_{\rm Atom}^{\rm init}$ is then (similar to Equation (7))

$$M_{\rm Atom}^{\rm init} = \rho_{\rm Atom} \times \frac{4}{3}\pi R_{\rm circ}^3,$$

$$\frac{M_{\rm Atom}^{\rm init}}{M_\odot} = 41.6\left(\frac{I_{\rm H\,I}}{500\ {\rm K\ km\ s}^{-1}}\right)\left(\frac{R_{\rm circ}}{10\ {\rm pc}}\right)^3. \quad (11)$$

$M_{\rm Atom}^{\rm init}$ is roughly 2 orders of magnitude lower than $M_{\rm Mol}^{\rm init}$ (Figure 2 and Table 1).

To estimate the dark matter contribution to the dynamical mass of H II regions, we compare the typical dark matter density $\rho_{\rm DM}$ between 1 and 10 kpc with the baryonic components estimated so far. For a subset of our targets, recent observational constraints on their dark matter density profiles are available from V. Vijayakumar et al. (2025). This work suggests $\rho_{\rm DM} \approx 10^{-1}$–$10^{-2}\ M_\odot\ {\rm pc}^{-3}$ at $R_{\rm gal} = 1$ kpc and $\approx10^{-2}$–$10^{-3}\ M_\odot\ {\rm pc}^{-3}$ at $R_{\rm gal} = 10$ kpc, within which 95% of our H II regions lie. This is consistent with simulation predictions for massive star-forming halos (see, e.g., A. Di Cintio et al. 2014; F. Jiang et al. 2023). Given that these

[43] Since there is no consensus on the functional form of the vertical stellar distribution in galaxies, we adopt the exponential form, which is in slightly better agreement with observations that often show profiles more centrally concentrated than sech^2 (e.g., P. S. Dobbie & S. J. Warren 2020; C. J. Jog 2025). Adopting a sech^2 profile instead (as in H. Salo et al. 2015) would predict 0.5 times the $\rho_{\rm Old}$ at the midplane, although both profiles agree at large z (see J. Sun et al. 2020).

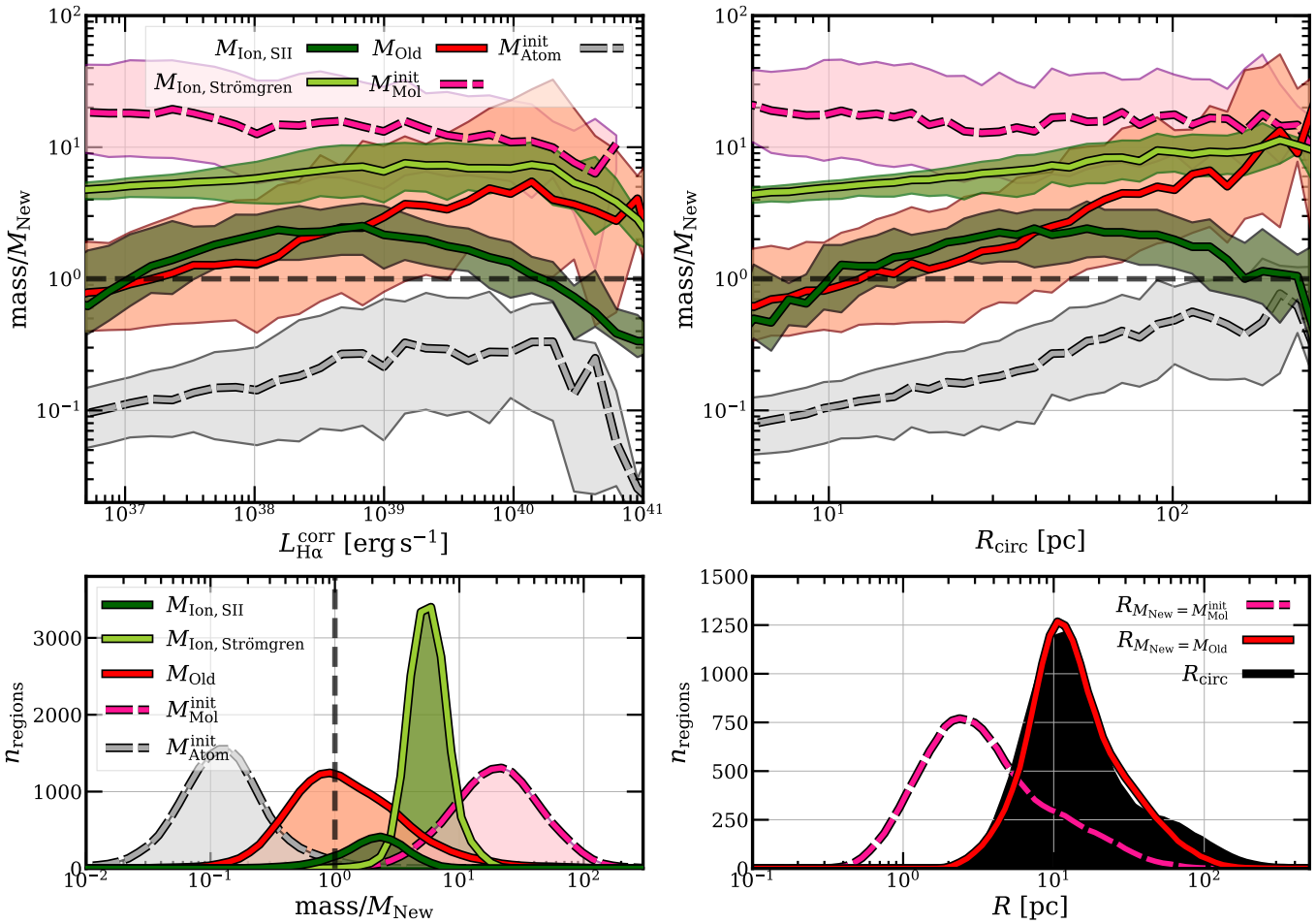

Figure 2. Variation in the different mass components relative to the young cluster mass $M_{\rm New}$ for the full sample of H II regions, binned in $L_{\rm H\alpha}{}^{\rm corr}$ (top left) and $R_{\rm circ}$ (top right) and summarized as histograms (bottom left). $M_{\rm Ion,\,S\,II}/M_{\rm New}$ (dark green), $M_{\rm Ion}$, Strömgren$/M_{\rm New}$ (light green), $M_{\rm Old}/M_{\rm New}$ (red), $M^{\rm init}_{\rm Mol}/M_{\rm New}$ (dashed pink), and $M^{\rm init}_{\rm Atom}/M_{\rm New}$ (dashed gray) are included for comparison. The dashed line indicates where a mass component is equal to $M_{\rm New}$. The bottom right panel includes the distribution of the measured $R_{\rm circ}$ (black), the estimated radius at which $M_{\rm New} = M^{\rm init}_{\rm Mol}$ (dashed pink), and the radius where $M_{\rm New} = M_{\rm Old}$ (red).

numbers are roughly 1 order of magnitude lower than $\rho_{\rm Atom}$ (see Table 2), we do not expect dark matter to contribute appreciably to the total mass of H II regions.

Finally, the average density of X-ray-emitting hot gas in galaxy disks is $n_{\rm e,\,X} \approx 10^{-3}$–$10^{-2}$ cm^{-3} (see, e.g., S. Mineo et al. 2012), which translates to $\rho_{\rm X} \approx 3 \times 10^{-5}$–$3 \times 10^{-4}\,M_\odot$ pc^{-3}, and is therefore negligible.

3. Results

3.1. Contribution of Ionized Gas and Older Stars

In Figures 1 and 2, we show the masses for our sample, which we summarize in Table 1 (see also Table 2 in the Appendix). These show that ionized gas and older stars contribute significantly to the masses of H II regions. After taking these into account, the mass of young stars, $M_{\rm New}$, only accounts for ≈10%–15% of the current mass in a region, on average. This is in excellent agreement with hydrodynamic simulations of star cluster formation and radiation feedback in turbulent molecular clouds (see, e.g., J.-G. Kim et al. 2018; S. H. Menon et al. 2025).

Ionized gas contributes significant mass to H II regions. Adopting the Strömgren sphere model, the ionized gas mass is typically $5 \times M_{\rm New}$ (Table 1). If instead we adopt the value of the electron density implied by the [S II] doublet, then the ionized gas mass is $\approx 2 \times M_{\rm New}$ (Section 2.1.2). We thus expect that the range $M_{\rm Ion} = 2$–$5 M_{\rm New}$ captures the true value, once again in agreement with cloud-scale simulations (see J.-G. Kim et al. 2018, 2021).

Thus, typical H II regions contain large reservoirs of gas that has been ionized by presupernova feedback but not yet cleared from the regions. Models of feedback in star-forming regions (e.g., D. Rahner et al. 2019; M. Y. Grudić et al. 2022; L. Lancaster et al. 2025) should reproduce this reservoir.

Because $M_{\rm New} \propto L_{\rm H\alpha}{}^{\rm corr}$ and $M_{\rm Ion} \propto L_{\rm H\alpha}{}^{\rm corr}/n_{\rm e}$, denser regions will have lower $M_{\rm Ion}/M_{\rm New}$. Equating Equations (1) and (5) yields $n_{\rm e} = 81$ cm^{-3} as the density needed to balance $M_{\rm New} = M_{\rm Ion}$. For any region with higher $n_{\rm e}$, $M_{\rm New} > M_{\rm Ion}$. Most regions in PHANGS-MUSE appear to have low $n_{\rm e}$ and hence large ionized gas masses, but density-sensitive spectroscopy targeting high-redshift sources suggests much higher $n_{\rm e} \sim 10^2$–10^3 cm^{-3} (e.g., M. W. Topping et al. 2025). If these spectroscopically inferred densities reflect the volume-averaged values, then $M_{\rm Ion}$ will be much less important for the mass budget of these systems.

H II regions are often considered as ionized nebulae surrounding young stars. In addition to the large reservoirs of ionized gas, our results indicate that for most ∼10 pc H II

regions, $M_{\rm Old} \approx M_{\rm New}$. Because $\rho_{\rm Old} \approx$ constant near each region and $M_{\rm new}$ is fixed by $L_{\rm H\alpha}$, the relative importance of the new and older stellar mass depends on the size scale considered. Figure 2 shows that the relative importance of the stellar mass terms changes from $M_{\rm New} \gtrsim M_{\rm Old}$ for small, low-luminosity regions to $M_{\rm Old} > M_{\rm New}$ for larger regions or regions in dense environments like galaxy centers.

By contrasting $M_{\rm New}$ with the expression for $M_{\rm Old}$, we can identify the scale above which older stars dominate the stellar mass in H II regions. Equating Equations (1) and (8), we estimate the size at which we expect $M_{\rm New} = M_{\rm Old}$ for each region, included in the bottom right panel of Figure 2. For our sample, the stellar masses balance at median $R = 12$ pc (16th–84th percentile $R \approx$ 7–27 pc), and we expect $M_{\rm Old} \gtrsim M_{\rm New}$ on larger scales than this, as previously highlighted in I. Blackstone & T. A. Thompson (2023). Thus, the mass of older stars is already significant on the ∼10 pc scales of H II regions resolved by HST and may become a more relevant term as a region is dispersed or evolves into a larger-scale bubble (e.g., O. V. Egorov et al. 2023; E. J. Watkins et al. 2023). While older stars do not necessarily dominate the overall mass budget on these scales (they have comparable or lower mass than molecular and ionized gas on scales $\lesssim$100 pc), they represent an important mass component.

3.2. Star Formation Efficiencies

In Figure 2, our estimated initial molecular mass generally exceeds all other components, and $M_{\rm Ion}$ exceeds $M_{\rm New}$. These results indicate the well-known inefficiency of converting gas into stars. The comparison of $M_{\rm New}$ with the initial gas mass before star formation allows us to estimate the star formation efficiencies (SFE) ϵ in each region. ϵ is defined as the fraction of gas mass converted into stars during the formation of the H II region (following, e.g., C. F. McKee & E. C. Ostriker 2007):

$$\epsilon = \frac{M_{\rm New}}{M_{\rm Cloud}^{\rm init}}. \quad (12)$$

Upper limit on ϵ from $M_{\rm Ion}$. The initial cloud mass $M_{\rm Cloud}^{\rm init}$ for an individual region can be difficult to constrain, but the current mass of the region $M_{\rm Ion} + M_{\rm New}$ represents a reasonable lower limit under the assumption that no mass has been lost from the region and all of the initial cold gas mass has been converted into stars or photoionized. As shown in Table 1 and Figure 3, contrasting $M_{\rm New}$ and $M_{\rm Ion} + M_{\rm New}$ provides an upper limit on the cluster-scale $\epsilon \approx$ 17%–36% (consistent with, e.g., C. J. Lada & E. A. Lada 2003).

Lower limit on ϵ from $M_{\rm Mol}^{\rm init}$. We also contrast $M_{\rm New}$ with our estimated initial molecular gas mass, $M_{\rm Mol}^{\rm init}$. This estimate will include any gas that has been cleared from the region or still remains in the molecular or atomic phase. This calculation yields a minimum $\epsilon \approx 6\%$ with ∼1 dex scatter. This is in line with recent estimates of molecular-cloud-scale ϵ (e.g., M. Chevance et al. 2020; J.-G. Kim et al. 2021; J. Kim et al. 2022; J. Sun et al. 2023; J. W. Zhou et al. 2025).

Alternatively, folding in the current molecular gas around each region and setting $M_{\rm Cloud}^{\rm init} = M_{\rm New} + M_{\rm Ion} + M_{\rm Mol}^{\rm current}$ (Figure 3, middle row, left panel) again yields $\epsilon \approx$ 6%–8%, consistent with using the full $M_{\rm Mol}^{\rm init}$.

Lower limit on ϵ from $M_{\rm Mol}^{\rm init}$. In Figure 3 (bottom row, right), we also compare the current $\Sigma_{\rm mol}$ toward each H II region to the mass-weighted 1.5 kpc average, $\langle\Sigma_{\rm Mol}\rangle_{150}$ (which we use to estimate $M_{\rm Mol}^{\rm init}$). H II regions show lower $\Sigma_{\rm Mol}$ compared to the average $\langle\Sigma_{\rm Mol}\rangle$ in their surroundings, median $\Sigma_{\rm Mol}/\langle\Sigma_{\rm Mol}\rangle_{150} \approx 0.62$. This statistical depletion of molecular gas toward H II regions provides another piece of evidence for molecular gas clearing by early stellar feedback (notably, ≈10% of our H II regions have no local CO detection at 150 pc). This allows us to estimate the amount of molecular gas "missing" from the region due to either star formation or feedback, $M_{\rm Mol}^{\rm init} - M_{\rm Mol}^{\rm current} \approx 0.38 M_{\rm Mol}^{\rm init}$, with the mass definition following Equation (9).[44]

As a test, we repeat the calculation of $\Sigma_{\rm Mol}/\langle\Sigma_{\rm Mol}\rangle$ at increasing physical resolution, from 150 pc (fiducial) to 90 pc and 60 pc (with higher-resolution data available only for smaller samples). Figure 3 (bottom right panel) shows that the higher-resolution measurements yield qualitatively similar results for local depletion of molecular gas at the locations of H II regions. $\Sigma_{\rm Mol}/\langle\Sigma_{\rm Mol}\rangle$ near H II regions steadily drops from 0.62, to 0.60, to 0.53 as the resolution improves from 150, to 90, to 60 pc, respectively. This also implies a statistical constraint on the amount of molecular gas that could be present in a shell around H II regions. At 60 pc resolution (our best CO(2–1) resolution), the median current molecular gas mass for our sample is $\lesssim 0.5 M_{\rm Mol}^{\rm init}$. This fraction of molecular gas remaining around H II regions should evolve over time and is expected to be larger than our sample median at earlier times.

Considering only the depleted molecular gas as the likely initial material for the H II region, $M_{\rm New}/(M_{\rm Mol}^{\rm init} - M_{\rm Mol}^{\rm current})$, the median ϵ is ∼9% at 150 pc resolution, 7% at 90 pc resolution, and 5% at 60 pc resolution.

Photoionization or gas clearing? Contrasting $M_{\rm Ion}$ with $M_{\rm Mol}^{\rm init}$ allows us to estimate the relative importance of photoionization and gas clearing for these regions. The current $M_{\rm New} + M_{\rm Ion}$ accounts for ≈33% of the initial gas mass $M_{\rm Mol}^{\rm init} + M_{\rm Atom}^{\rm init}$, as shown in the bottom left panel of Figure 3. This suggests that on average, ≈67% of the original gas has either been dispersed from the region or still resides in the cold phase (perhaps in shells). The other 33% remains mostly as photoionized gas.

We can refine this estimate, as above, by contrasting $M_{\rm New} + M_{\rm Ion}$ with the molecular gas depleted toward H II regions, $M_{\rm Mol}^{\rm init} - M_{\rm Mol,150}^{\rm current}$. $M_{\rm New} + M_{\rm Ion}$ accounts for ≈55% of this depleted mass. In this case, about half of the molecular gas statistically estimated to be depleted is still visible as ionized gas and new stars, while half has been cleared.

Variation in ϵ with $\langle\Sigma_{\rm Mol}\rangle$. From theoretical models, ϵ is expected to relate to the initial gas surface density $\Sigma_{\rm Cloud}^{\rm init}$ of the molecular cloud core out of which a H II region is born (e.g., S. Raskutti et al. 2016; T. A. Thompson & M. R. Krumholz 2016; J.-G. Kim et al. 2018, 2021; M. Y. Grudić et al. 2019; C.-C. He et al. 2019; H. Fukushima et al. 2020; L. Lancaster et al. 2021; S. H. Menon et al. 2022, 2023; M. Chevance et al. 2023 and references therein). Clouds with higher initial surface density are expected to convert more of their material to stars.

The middle row, right panel in Figure 3 shows several ϵ estimates as a function of $\langle\Sigma_{\rm Mol}\rangle_{150\,\rm pc}$. The figure shows different trends for each approach, reflecting both correlated axes (for ϵ estimates involving $M_{\rm Mol}^{\rm init}$) and the difficulty of

[44] Note that the appropriate geometry to translate $\Sigma_{\rm Mol}/\langle\Sigma_{\rm Mol}\rangle_{150}$ into a missing mass associated with the H II region is ambiguous. While we use the region size, $\pi R_{\rm circ}^2(\langle\Sigma_{\rm Mol}\rangle_{150} - \Sigma_{\rm Mol})$, one could also consider the whole ALMA beam rather than a surface density estimate.

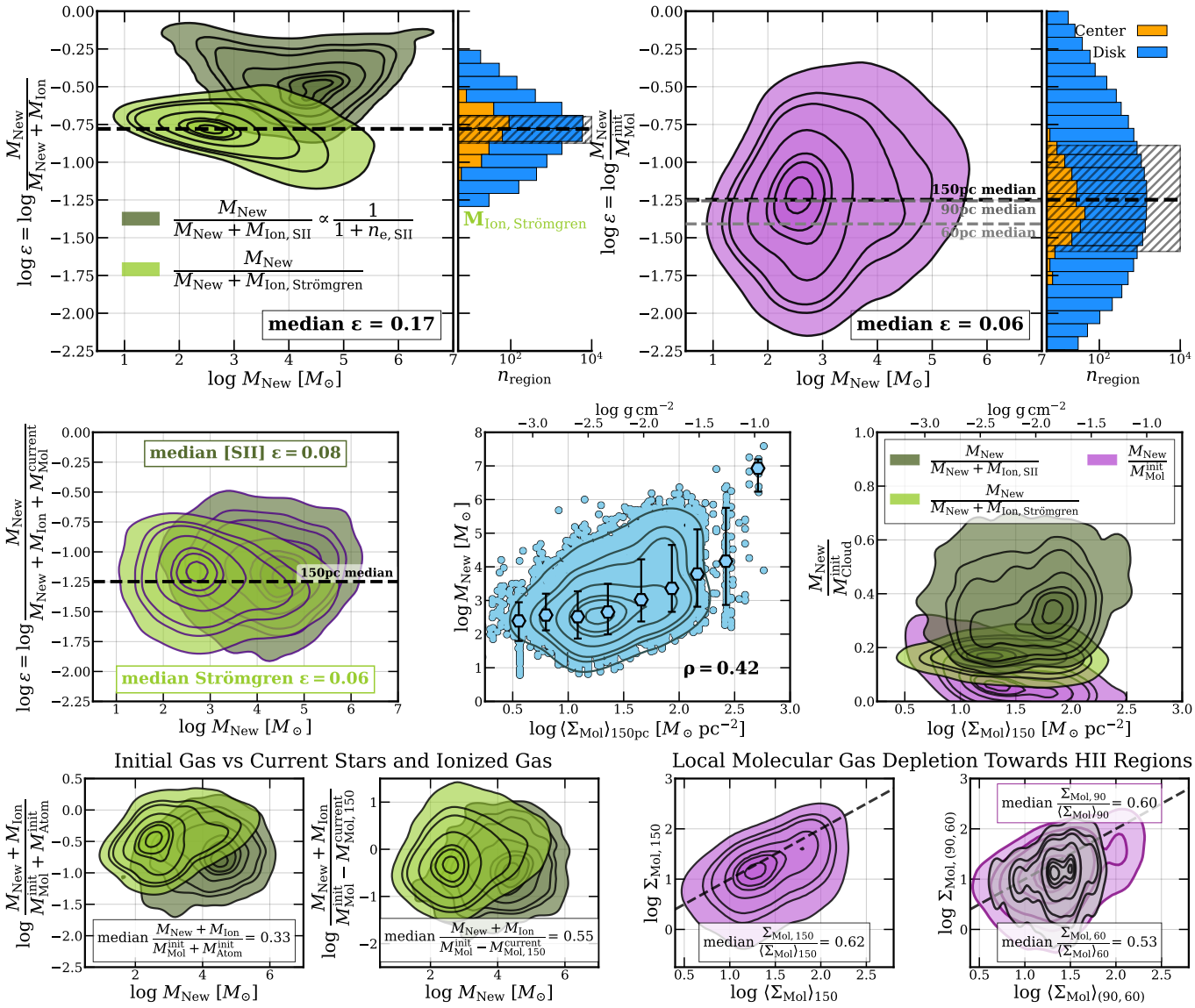

Figure 3. Top: summarizing H II region-scale SFEs. Data density contours for the 5th/16th/25th/50th/75th/84th/95th percentile SFE using $M_{\rm Ion,S\ II}$ (dark green), $M_{\rm Ion}$, Strömgren (light green), and $M_{\rm Mol}^{\rm init}$ (purple). The full histogram and medians as before (dashed line) for $M_{\rm Ion}$, Strömgren and $M_{\rm Mol}^{\rm init}$ are included. We also include the medians using $M_{\rm Mol}^{\rm init}$ at 90–60 pc resolution. Middle: from left to right, the fraction of current gas and stars in young stars, the moderate correlation (Spearman $\rho = 0.42$) and large scatter between $M_{\rm New}$ and $\langle\Sigma_{\rm Mol}\rangle_{150\,\rm pc}$, and three estimates of $M_{\rm New}/M_{\rm Cloud}$ vs. $\langle\Sigma_{\rm Mol}\rangle_{150\,\rm pc}$. Bottom: from left to right, the fraction of initial gas seen in stars and ionized gas, the fraction of depleted initial molecular gas in stars and ionized gas, the statistical local depletion in molecular gas toward H II regions at our fiducial 150 pc resolution, and finally, the depletion for smaller samples (where available) at 90 pc (purple) and 60 pc (gray) resolution, relative to the dashed black 1:1 line.

estimating $M_{\rm Mol}^{\rm init}$ for any given region. Still, given the relatively low surface densities in our sample, the modest ϵ observed appears to be in agreement with predictions of efficiencies well below 1 (e.g., T. A. Thompson & M. R. Krumholz 2016). Improving estimates of the initial mass and ϵ represent a goal for future work. For a related exercise focused on the gas depletion time, $M_{\rm Mol}^{\rm init}$/SFR, to region-averaged cloud properties, see A. K. Leroy et al. (2025) or S. E. Meidt et al. (2025).

3.3. Dynamical Evolution of Regions

Based on our mass measurements, we provide estimates of the dynamical state of H II regions. With the enclosed mass $M_{\rm Enclosed} = M_{\rm New} + M_{\rm Ion}$, Strömgren + $M_{\rm Old}$ within $R_{\rm circ}$, we first estimate the escape velocity for gas, $v_{\rm esc}$, as

$$v_{\rm esc} = \left(\frac{2GM_{\rm Enclosed}}{R_{\rm circ}}\right)^{1/2} = 2.1\left(\frac{M_{\rm Enclosed}}{5000\,M_\odot}\right)^{1/2}\left(\frac{R_{\rm circ}}{10\ \rm pc}\right)^{-1/2}\ \rm km\ s^{-1}. \quad (13)$$

We calculate a median H II region $v_{\rm esc} = 1.8\,\rm km\,s^{-1}$, which rises to $\approx$50 km s^{-1} for the brightest regions in galaxy centers (Figure 4; see also Table 2). Comparing to the typical sound speed $c_{\rm s} \approx 11.6$ km s^{-1} for 10,000 K warm gas or the typical rms warm gas velocity $v_{\rm rms} \approx \sqrt{3}\,c_{\rm s} \approx 20$ km s^{-1}, on average, $v_{\rm esc} < v_{\rm rms}$.

However, $v_{\rm esc}$ alone is not enough to determine whether H II regions are underpressured (and hence collapsing), in equilibrium, or overpressured (expanding). H II regions evolve in the context of

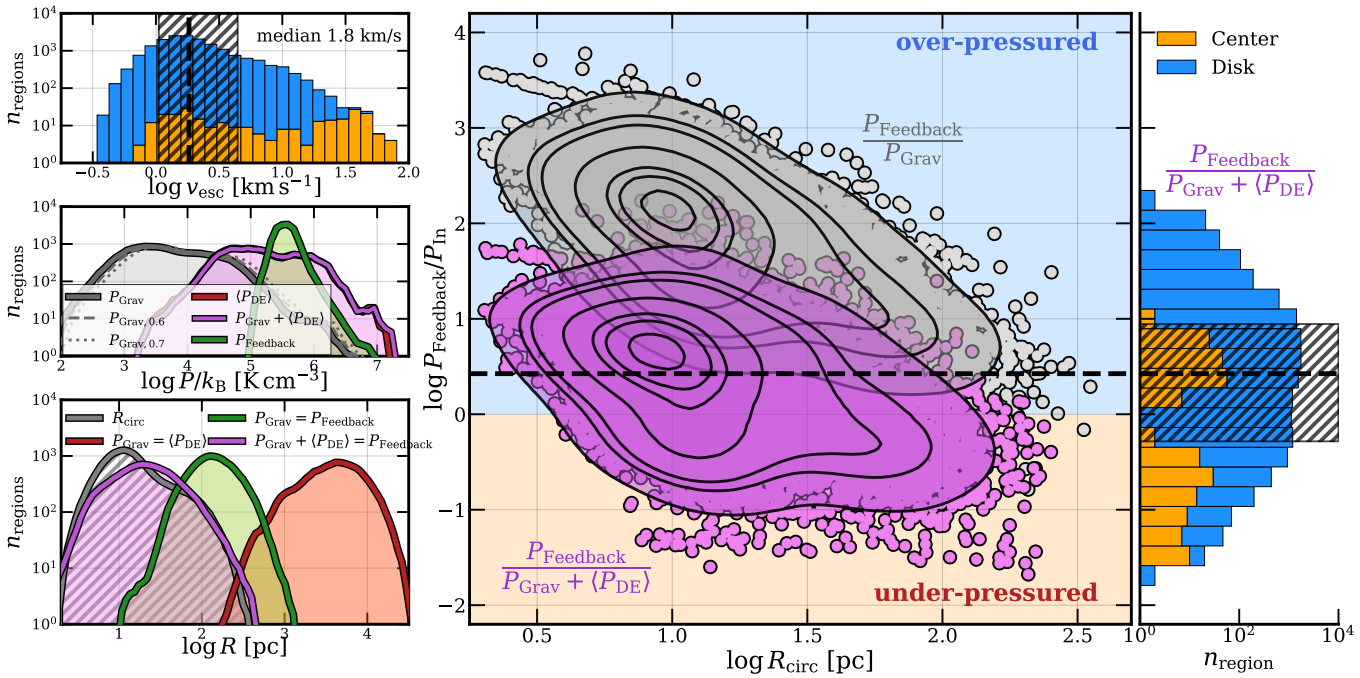

Figure 4. Top left: distribution of H II region escape velocities in galaxy centers and disks. Middle left: distribution of pressures due to H II region self-gravity for $M_{\rm sh} = 50\%M_{\rm Mol}^{\rm init}$ (fiducial value; solid gray), $60\%M_{\rm Mol}^{\rm init}$ (dashed gray), and $70\%M_{\rm Mol}^{\rm init}$ (dotted–dashed gray); disk $\langle P_{\rm DE}\rangle$ (from J. Sun et al. 2023; maroon); fiducial $P_{\rm Grav}+\langle P_{\rm DE}\rangle$ (purple), and total $P_{\rm Feedback}$ (green). Bottom left: distribution of H II region $R_{\rm circ}$ (gray hatches) and the sizes at which we expect $P_{\rm Grav}=\langle P_{\rm DE}\rangle$ (maroon), $P_{\rm Grav}=P_{\rm Feedback}$ (green), and $P_{\rm Grav}+\langle P_{\rm DE}\rangle=P_{\rm Feedback}$ (purple). Right: H II region overpressure (shaded blue) vs. underpressure (shaded orange) for $P_{\rm Feedback}/P_{\rm Grav}$ (gray) and $P_{\rm Feedback}/(P_{\rm Grav}+\langle P_{\rm DE}\rangle)$ (purple; the dashed line indicates the median, with a summary histogram to the right) with 5th/16th/25th/50th/75th/84th/95th percentile contours.

their local galactic environment, and a balance of gravity, the ambient ISM pressure $P_{\rm ext}$, and total feedback pressure determines their evolution. The relevant quantity here is the momentum equation for the shell of swept-up material (e.g., N. Murray et al. 2010; D. Rahner et al. 2017, 2019; L. Lancaster et al. 2025), which we write here terms of pressure on a thin shell of radius $R_{\rm circ}$,

$$\frac{1}{4\pi R_{\rm circ}^2}\frac{dp_{\rm sh}}{dt} = -P_{\rm Grav} - P_{\rm ext} + P_{\rm Feedback},$$
$$= -\frac{GM_{\rm sh}\left(M_{\rm Enclosed}+\frac{1}{2}M_{\rm sh}\right)}{R_{\rm circ}^2(4\pi R_{\rm circ}^2)} - \langle P_{\rm DE}\rangle$$
$$+ (P_{\rm Therm}+P_{\rm Rad}+P_{\rm Wind}+P_{\rm X}). \quad (14)$$

Here $p_{\rm sh}$ is the momentum of a thin gaseous shell (thickness $\ll R_{\rm circ}$) of mass $M_{\rm sh}$. We set $M_{\rm sh}$ to $0.5M_{\rm Mol}^{\rm init}$ since, on average, $\sim$50% of the initial molecular gas is locally depleted (see Section 3.2).[45] $P_{\rm Grav}$ is a pressure-like gravity term that accounts for the shell's response to the gravitational force exerted by the mass enclosed by the thin gaseous shell [46] as well as the self-gravity of the shell material itself. For the external ISM pressure, we use the 1.5 kpc average flux-weighted 150 pc-scale galactic disk dynamical equilibrium pressure $P_{\rm ext} = \langle P_{\rm DE}\rangle$ from the J. Sun et al. (2022, 2023) megatables.

We contrast these inward pressure terms ($P_{\rm Grav}$ and $\langle P_{\rm DE}\rangle$) with the combined presupernova feedback from young stars, $P_{\rm Feedback}$. This includes the warm gas pressure $P_{\rm Therm}$ and the total radiation pressure $P_{\rm Rad}$ from both UV and IR photons computed for this sample of regions in D. Pathak et al. (2025), as well as first-order estimates for the pressure due to stellar winds $P_{\rm Wind}$ (assuming a momentum-conserving wind; see also A. T. Barnes et al. 2021; L. Lancaster et al. 2025) by scaling the luminosity-weighted STARBURST99 stellar wind outputs averaged over the first 4 Myr of SSP evolution as

$$\frac{P_{\rm Wind}}{k_{\rm B}} = \frac{\sqrt{2\dot{M}_{\rm Wind}L_{\rm mech}}}{4\pi R_{\rm circ}^2 k_{\rm B}}$$
$$= 7.7\times10^3\left(\frac{L_{\rm H\alpha}{}^{\rm corr}}{10^3\,L_\odot}\right)\left(\frac{R_{\rm circ}}{10\ {\rm pc}}\right)^{-2}{\rm K\ cm^{-3}}. \quad (15)$$

Finally, we include a constant X-ray pressure for 0.2 keV and $n_{\rm e,\,X} = 5\times10^{-3}\,{\rm cm^{-3}}$ hot gas (e.g., S. Mineo et al. 2012) as

$$\frac{P_{\rm X}}{k_{\rm B}} = 2n_{\rm e,\,X}T_{\rm X} = 2.3\times10^4\ {\rm K\ cm^{-3}}. \quad (16)$$

This sets a minimum pressure ($\ll P_{\rm Therm}$) due to diffuse, X-ray-emitting hot gas to account for the thermal pressure from shock-heated gas by supernovae and stellar winds. While follow-up work will present more rigorous estimates of $P_{\rm Wind}$ and $P_{\rm X}$, this is a reliable first-order estimate that includes the

[45] On average, $\approx$50% of the molecular gas in a beam toward the H II region appears depleted. We assume that the gas around the region itself has been cleared by a similar factor, with the remaining gas in a shell around the region, and so adopt $M_{\rm sh} = 0.5\times M_{\rm Mol}^{\rm init}$. Given the coarse resolution of the ALMA data, we consider this more reliable than $M_{\rm Mol}^{\rm current}$ but note this as a direction where future higher-resolution observations will improve our view.

[46] We take the evolution of the gaseous shell as representative of the evolution of the H II region. When the shell is static, we take this as an indication that the H II region is in equilibrium. This occurs when the outward pressure force is balanced by the gravitational force inward and the external compressive "weight" of gas and stars in a *finite* galaxy disk. For any realistically finite disk, the density effectively goes to zero at some large (but finite) distance L. For H II regions in a stellar disk, $R_{\rm circ} \ll h_z^{\rm exp} \ll L$, and Gauss's law for gravitation applies as long as L is finite. Hence, $g = -GM_{\rm Enclosed}/R_{\rm circ}^2$ on the shell. For a more detailed derivation of $P_{\rm Grav}$, refer to Section 2 and Appendix A in J. P. Ostriker & C. F. McKee (1988).

dominant feedback terms in optically bright H II regions, where $P_{\rm Therm}/k_{\rm B} \approx 5 \times 10^5\,{\rm K\,cm^{-3}}$ primarily drives the total $P_{\rm Feedback}$ (L. A. Lopez et al. 2014; A. T. Barnes et al. 2021, 2025; D. Pathak et al. 2025).

In Figure 4, we summarize $P_{\rm Grav}$ and $\langle P_{\rm DE}\rangle$ (inward pressure) against $P_{\rm Feedback}$ (outward pressure). The distributions show that generally, $\langle P_{\rm DE}\rangle \gg P_{\rm Grav}$; i.e., the ambient ISM pressure is the major term opposing feedback, and gravity plays a subdominant role at this scale. Varying $M_{\rm sh}$ from $0.5M_{\rm Mol}^{\rm init}$ (fiducial) to 0.6 and $0.7M_{\rm Mol}^{\rm init}$ increases $P_{\rm Grav}$ by roughly 30% and 60% but is still not enough for $P_{\rm Grav}$ on the gaseous shell to be significant compared to external $\langle P_{\rm DE}\rangle$. In fact, given the local ${L_{\rm H\alpha}}^{\rm corr}$, $\langle\Sigma_{\rm Mol}\rangle$, and $\rho_{\rm Old}$, the minimum scales at which we expect $P_{\rm Grav} \approx \langle P_{\rm DE}\rangle$ are large, typically a few kiloparsecs (see Table 2).

While $P_{\rm Grav} \ll \langle P_{\rm DE}\rangle$, we can still calculate at what scales gravity alone might be comparable to feedback. We expect $P_{\rm Grav} \approx P_{\rm Feedback}$ at 130 pc scales (Figure 4, bottom left). This scale is smaller (median 60 pc) for high-density regions in galaxy centers. By contrast, for most regions, we expect $P_{\rm Grav} + \langle P_{\rm DE}\rangle \approx P_{\rm Feedback}$ at ≈20–30 pc scales, which is $\sim R_{\rm circ}$ (Table 2).

We calculate the factor by which regions are "overpressured," $P_{\rm Feedback}/(P_{\rm Grav} + \langle P_{\rm DE}\rangle)$. Values >1 (or log "overpressure" >0 in Figure 4) indicate regions that are expanding. The majority (71%) of our H II regions are overpressured (expanding), especially smaller regions. Larger regions, especially those in galaxy centers, experience higher $\langle P_{\rm DE}\rangle$ and $P_{\rm Grav}$ and hence become underpressured despite higher $P_{\rm Feedback}$ (see also A. T. Barnes et al. 2021).

Finally, we compare the "overpressure" with the R at which we expect $P_{\rm Feedback} = P_{\rm Grav} + \langle P_{\rm DE}\rangle$ (R≈20 pc), and the current $R_{\rm circ}$ of each region, which confirms that overpressure/underpressure corresponds to different stages of H II region evolution—early or late—depending on environment (Table 2).

4. Summary

Combining high-resolution MUSE optical spectral mapping, HST Hα narrowband imaging, JWST near-IR imaging, and ALMA CO data with VLA and MeerKAT 21 cm data, we measure the masses of ∼18,000 H II regions across 19 nearby star-forming galaxies at 10 pc physical resolution, including the mass of the young cluster (Section 2.1.1), ionized gas (Section 2.1.2), coincident old stars from the disk (Section 2.1.3), initial molecular gas (Section 2.2.1), and atomic gas (Section 2.2.2), as well as bounds on the dark matter and hot gas mass (Section 2.2.2). These represent the first comprehensive estimates of H II region masses and self-gravity for a statistically large set of regions outside the Local Group. Our mass estimates have direct implications for the efficiency of stellar feedback in ionizing and clearing cold gas and the dynamical evolution of H II regions, summarized as follows.

1. The mass of ionized gas in H II regions is significant, $M_{\rm Ion} = 2$–$5 \times M_{\rm New}$, depending on the method used to estimate the ionized gas density (Figures 1 and 2, Table 1, Section 3.1). Models of stellar feedback in H II regions should reproduce significant reservoirs of photoionized but not yet cleared gas.
2. On the 10 pc scale of individual regions, the mass of older stars associated with the stellar disk is already comparable to $M_{\rm New}$ (Figures 1 and 2, Table 1, Section 3.1). Older stars become an increasingly significant enclosed mass term at larger scales and in high stellar density environments like galaxy centers.
3. A conservative upper limit of ≈17%–35% for the SFE is obtained by comparing the current mass of young stars and ionized gas, while a lower limit of ≈6% results from combining the initial molecular gas and current young stellar mass. The sites of H II regions show a ≈40%–50% depletion in molecular gas relative to the typical surface density in the surrounding region (Section 3.2, Figure 3).
4. We compare the effect of gravity to the ISM pressure expected from dynamical equilibrium. When accounting for the full enclosed mass, self-gravity always plays a secondary role relative to external pressure in confining regions. Comparing inward and outward pressures, we find that most $R_{\rm circ} \sim 10$ pc regions are overpressured relative to their self-gravity and their surroundings and so are likely to expand, while larger regions in galaxy centers appear to be confined (Figure 4, Section 3.3). Region self-gravity is expected to dominate over feedback pressure at ≈130 pc scales but always remains subdominant to the ambient ISM pressure.

Acknowledgments

We thank the anonymous referee for the constructive feedback.

This work has been carried out as part of the PHANGS collaboration. This work is based on observations made with the NASA/ESA/CSA JWST. The data were obtained from the Mikulski Archive for Space Telescopes (MAST) at the Space Telescope Science Institute, which is operated by the Association of Universities for Research in Astronomy, Inc., under NASA contract NAS 5-03127 for JWST. These observations are associated with program 2107. The specific JWST observations analyzed can be accessed via the MAST PHANGS-JWST High Level Science Product, doi:10.17909/ew88-jt15, and the HST data can be accessed through the MAST PHANGS-HST High Level Science Product, doi:10.17909/t9-r08f-dq31. The PHANGS-MUSE LP data can be accessed at ESO, doi:10.18727/archive/47.

This work is also based on observations collected at the European Southern Observatory under ESO programs 094.C-0623 (PI: Kreckel), 095.C-0473, 098.C-0484 (PI: Blanc), 1100.B-0651 (PHANGS-MUSE; PI: Schinnerer), 094.B-0321 (MAGNUM; PI: Marconi), 099.B-0242, 0100.B-0116, 098.B-0551 (MAD; PI: Carollo), and 097.B-0640 (TIMER; PI: Gadotti).

This paper makes use of MeerKAT observations. The MeerKAT telescope isoperated by the South African Radio Astronomy Observatory, which is a facility of the National Research Foundation, an agency of the Department of Science and Innovation.

D.P. is supported by the NSF GRFP.

A.K.L. and D.P. gratefully acknowledge support from NSF AST AWD 2205628, JWST-GO-02107.009-A, and JWST-GO-03707.001-A. A.K.L. also gratefully acknowledges support by a Humbolt Research Award.

L.A.L. acknowledges support through the Heising-Simons Foundation grant 2022-3533.

J.S. acknowledges support by the National Aeronautics and Space Administration (NASA) through the NASA Hubble Fellowship grant HST-HF2-51544 awarded by the Space Telescope Science Institute (STScI), which is operated by the Association of Universities for Research in Astronomy, Inc., under contract NAS 5-26555.

D.J.P. greatly acknowledges support from the South African Research Chairs Initiative of the Department of Science and Technology and National Research Foundation.

M.B. acknowledges support from the ANID BASAL project FB210003. This work was supported by the French government through the France 2030 investment plan managed by the National Research Agency (ANR), as part of the Initiative of Excellence of Université Côte d'Azur under reference number ANR-15-IDEX-01.

Z.B. and D.C. gratefully acknowledge the Collaborative Research Center 1601 (SFB 1601 subproject B3) funded by the Deutsche Forschungsgemeinschaft (DFG, German Research Foundation) - 500700252. D.C. acknowledges support by the Deutsche Forschungsgemeinschaft, DFG project number SFB 956-A3.

K.G. is supported by the Australian Research Council through the Discovery Early Career Researcher Award (DECRA) Fellowship (project number DE220100766) funded by the Australian Government.

E.R. acknowledges the support of the Natural Sciences and Engineering Research Council of Canada (NSERC), funding reference number RGPIN-2022-03499, and support from the Canadian Space Agency, funding reference 23JWGO2A07.

O.E. acknowledges funding from the Deutsche Forschungsgemeinschaft (DFG, German Research Foundation)—project ID 541068876.

P.S.B. acknowledges support from the Spanish grant PID2022-138855NB-C31, funded by MCIN/AEI/10.13039/501100011033/FEDER, EU.

R.S.K. acknowledges financial support from the ERC via Synergy Grant "ECOGAL" (project ID 855130), from the German Excellence Strategy via the Heidelberg Cluster "STRUCTURES" (EXC 2181—390900948), and from the German Ministry for Economic Affairs and Climate Action in project "MAINN" (funding ID 50OO2206).

Facilities: JWST, VLT:Yepun, HST, ALMA, VLA, MeerKAT.

Software: astropy (Astropy Collaboration et al. 2013, 2018).

Appendix
Summary of H II Region Properties

We provide a more detailed summary of HII region properties for reference in Table 2, and provide ancillary information for using the associated data file for the full HII region sample in Table 3.

Table 2
Summary of H II Region Properties

Quantity	Unit	Unweighted		$L_{H\alpha}{}^{corr}$-weighted		Notes
		All	Center	All	Center	
R_{circ}	pc	$11.92^{30.27}_{6.6}$	$22.36^{129.47}_{6.63}$	$124.26^{200.68}_{68.63}$	$142.47^{266.57}_{98.68}$	A. T. Barnes et al. 2025; see also B. Groves et al. (2023)
$L_{H\alpha}{}^{corr}$	$\log L_\odot$	$3.6^{4.67}_{2.92}$	$4.32^{6.47}_{2.93}$	$6.8^{8.0}_{5.7}$	$7.82^{8.38}_{7.18}$	…
n_e, Strömgren	cm^{-3}	$15.24^{19.16}_{11.78}$	$15.83^{20.93}_{10.83}$	$16.59^{55.56}_{8.68}$	$30.18^{160.09}_{16.28}$	Section 2.1.2
[a]$n_{e,\ S\ II}$	cm^{-3}	$42.33^{79.89}_{25.58}$	$106.45^{228.61}_{55.05}$	$130.43^{238.85}_{44.22}$	$185.17^{282.45}_{132.22}$	…
I_{F300M}	MJy sr^{-1}	$0.4^{0.92}_{0.2}$	$3.52^{9.47}_{1.65}$	$2.86^{13.23}_{0.49}$	$8.96^{17.54}_{3.08}$	Section 2.1.3
ρ_{Old}	$\log M_\odot$ pc^{-3}	$-1.04^{-0.65}_{-1.36}$	$-0.02^{0.37}_{-0.32}$	$-0.65^{-0.08}_{-1.05}$	$-0.32^{0.13}_{-1.03}$	…
$\langle\Sigma_{Mol}\rangle_{150}$	$\log M_\odot$ pc^{-2}	$1.52^{1.89}_{1.17}$	$1.52^{2.33}_{1.38}$	$2.04^{2.72}_{1.69}$	$2.72^{2.72}_{2.47}$	Section 2.2.1; J. Sun et al. (2022)
Σ_{Atom}	$\log M_\odot$ pc^{-2}	$1.01^{1.19}_{0.79}$	$0.74^{0.95}_{0.65}$	$1.03^{1.26}_{0.79}$	$0.8^{0.85}_{0.71}$	Section 2.2.2
ρ_{Atom}	$\log M_\odot$ pc^{-3}	$-1.99^{-1.81}_{-2.21}$	$-2.26^{-2.05}_{-2.35}$	$-1.97^{-1.74}_{-2.21}$	$-2.2^{-2.15}_{-2.29}$	…
M_{New}	$\log M_\odot$	$2.81^{3.88}_{2.12}$	$3.53^{5.68}_{2.13}$	$6.0^{7.2}_{4.9}$	$7.03^{7.59}_{6.38}$	Section 2.1.1; Figure 1
M_{Ion}, Strömgren	$\log M_\odot$	$3.5^{4.63}_{2.78}$	$4.3^{6.57}_{2.79}$	$6.76^{7.29}_{5.71}$	$7.27^{7.48}_{6.88}$	Section 2.1.2; Figure 1
[a]$M_{Ion,\ S\ II}$	$\log M_\odot$	$4.61^{5.33}_{3.51}$	$5.44^{6.01}_{4.86}$	$5.98^{6.84}_{5.3}$	$6.49^{7.37}_{5.91}$	…
M_{Old}	$\log M_\odot$	$2.8^{4.14}_{1.93}$	$4.61^{7.19}_{2.91}$	$6.33^{7.35}_{5.32}$	$6.97^{7.47}_{5.57}$	Section 2.1.3; Figure 1
M_{Mol}^{init}	$\log M_\odot$	$4.1^{5.12}_{3.33}$	$4.56^{6.71}_{3.43}$	$6.66^{7.51}_{5.81}$	$7.51^{8.06}_{7.35}$	Section 2.2.1; Figure 1
M_{Atom}^{init}	$\log M_\odot$	$1.83^{3.1}_{0.98}$	$2.29^{4.58}_{0.73}$	$4.78^{5.35}_{3.92}$	$5.02^{5.23}_{4.48}$	Section 2.2.2; Figure 1
$\frac{M_{Ion,\ Strömgren}}{M_{New}}$	…	$5.01^{6.48}_{3.99}$	$4.83^{7.05}_{3.65}$	$4.6^{8.8}_{1.38}$	$2.53^{4.69}_{0.48}$	Section 3.1; Figure 2
[a]$\frac{M_{Ion,\ S\ II}}{M_{New}}$	…	$1.89^{3.13}_{1.0}$	$0.75^{1.46}_{0.35}$	$0.61^{1.81}_{0.34}$	$0.43^{0.61}_{0.28}$	…
$\frac{M_{Old}}{M_{New}}$	…	$1.01^{3.1}_{0.41}$	$10.35^{52.96}_{3.55}$	$2.28^{9.78}_{0.24}$	$1.81^{11.19}_{0.01}$	…
$\frac{M_{Mol}^{init}}{M_{New}}$	…	$17.71^{39.0}_{7.74}$	$20.17^{32.52}_{10.96}$	$10.36^{21.0}_{3.07}$	$9.15^{15.01}_{1.25}$	…
[a]$\frac{M_{Ion,\ S\ II}}{M_{Ion,\ Strömgren}}$	…	$0.29^{0.47}_{0.17}$	$0.13^{0.25}_{0.07}$	$0.2^{0.46}_{0.08}$	$0.13^{1.27}_{0.07}$	…
$\frac{M_{Ion,\ Strömgren}}{M_{Mol}^{init}}$	…	$0.29^{0.66}_{0.13}$	$0.25^{0.48}_{0.17}$	$0.55^{0.88}_{0.32}$	$0.41^{0.85}_{0.32}$	…
$\log\frac{M_{Atom}^{init}}{M_{Mol}^{init}}$	…	$-2.22^{-1.77}_{-2.61}$	$-2.48^{-2.1}_{-2.76}$	$-1.7^{-1.29}_{-2.17}$	$-2.29^{-2.04}_{-2.53}$	…
$\frac{M_{New}}{M_{New}+M_{Ion,\ Strömgren}}$	…	$0.17^{0.2}_{0.13}$	$0.17^{0.22}_{0.12}$	$0.18^{0.42}_{0.1}$	$0.28^{0.68}_{0.18}$	Section 3.2; Figure 3
$\frac{M_{New}}{M_{Mol}^{init}}$	…	$0.06^{0.13}_{0.03}$	$0.05^{0.09}_{0.03}$	$0.1^{0.33}_{0.05}$	$0.11^{0.8}_{0.07}$	…

Table 2
(Continued)

Quantity	Unit	Unweighted		$L_{H\alpha}{}^{corr}$-weighted		Notes
		All	Center	All	Center	
$M_{Enclosed}$	$\log M_\odot$	$3.67^{4.83}_{2.93}$	$4.81^{7.33}_{3.15}$	$7.16^{7.76}_{5.96}$	$7.63^{7.91}_{7.32}$	Section 3.3; Figure 4; $\langle P_{DE}\rangle$ from J. Sun et al. (2022, 2023)
v_{esc}	km s^{-1}	$1.83^{4.43}_{1.05}$	$4.98^{38.06}_{1.4}$	$28.58^{54.68}_{10.42}$	$51.01^{70.87}_{37.8}$	⋯
P_{Grav}	log K cm^{-3}	$3.59^{4.39}_{3.03}$	$3.96^{5.8}_{3.43}$	$5.19^{6.47}_{4.48}$	$6.41^{6.98}_{6.07}$	⋯
$\langle P_{DE}\rangle$	log K cm^{-3}	$5.07^{5.79}_{4.54}$	$5.12^{6.22}_{4.85}$	$5.91^{6.33}_{5.34}$	$6.79^{6.97}_{6.22}$	⋯
$P_{Feedback}$	log K cm^{-3}	$5.49^{5.6}_{5.41}$	$5.54^{5.82}_{5.45}$	$5.93^{6.84}_{5.46}$	$6.42^{7.63}_{5.96}$	⋯
$\log \frac{P_{Feedback}}{P_{Grav}+\langle P_{DE}\rangle}$	⋯	$0.43^{0.95}_{-0.28}$	$0.35^{0.66}_{-0.8}$	$-0.26^{0.26}_{-0.71}$	$-0.97^{-0.6}_{-1.5}$	⋯
$R_{\langle P_{DE}\rangle=P_{Grav}}$	pc	$3746.75^{7503.73}_{1482.19}$	$572.23^{814.02}_{395.55}$	$514.7^{4169.61}_{9.29}$	$659.11^{1688.87}_{173.42}$	⋯
$R_{P_{Feedback}=P_{Grav}}$	pc	$127.8^{233.8}_{72.46}$	$61.04^{92.61}_{45.45}$	$190.43^{290.0}_{91.03}$	$62.24^{75.88}_{53.69}$	⋯
$R_{P_{Feedback}=P_{Grav}+\langle P_{DE}\rangle}$	pc	$19.06^{44.47}_{8.14}$	$14.39^{29.08}_{8.47}$	$34.67^{72.12}_{14.13}$	$13.15^{21.79}_{5.06}$	⋯
$\log \frac{R_{circ}}{R_{P_{Feedback}=P_{Grav}+\langle P_{DE}\rangle}}$	⋯	$-0.21^{0.3}_{-0.57}$	$-0.17^{0.7}_{-0.39}$	$0.43^{0.76}_{0.06}$	$1.14^{1.56}_{0.6}$	⋯

Notes. Summary of H II region properties and key results with references. The unweighted and $L_{H\alpha}{}^{corr}$-weighted median and 16th–84th percentile range (as $\text{median}^{84\text{th percentile}}_{16\text{th percentile}}$) for each quantity is presented for the full sample and for galaxy centers.
[a] From [S II] doublet $n_{e\ ,S\ II}$ for a subset of 3221 H II regions (see Section 2.1.2 for details).

Table 3
Columns in Value-added Catalog

Column	Unit	Description
Galaxy	⋯	Galaxy name
RegionID	⋯	Nebular region ID from B. Groves et al. (2023) and A. T. Barnes et al. (2025)
Env	⋯	Local environment following M. Querejeta et al. (2021)
Rcirc	pc	R_{circ} following A. T. Barnes et al. 2025 and D. Pathak et al. (2025)
LHacorr	erg s^{-1}	$L_{H\alpha}{}^{corr}$, estimated to match region size (A. T. Barnes et al. 2025; D. Pathak et al. 2025)
MNew	$M_\odot$	M_{New} (Section 2.1.1)
ne-Stromgren	cm^{-3}	n_e, Strömgren (Section 2.1.2)
ne-SII	cm^{-3}	$n_{e,\ S\ II}$ (Section 2.1.2)
MIon-Stromgren	$M_\odot$	M_{Ion}, Strömgren (Section 2.1.2)
MIon-SII	$M_\odot$	$M_{Ion,\ S\ II}$ (Section 2.1.2)
rhoOld	$M_\odot$ pc^{-3}	ρ_{Old} (Section 2.1.3)
MOld	$M_\odot$	M_{Old} (Section 2.1.3)
SigmaMol-hex-150pc	$M_\odot$ pc^{-2}	$\langle\Sigma_{Mol}\rangle_{150\ pc}$ from J. Sun et al. (2022) (Section 2.2.1)
MMol-init-150pc	$M_\odot$	M^{init}_{Mol} (Section 2.2.1)
MMol-current-150pc	$M_\odot$	$M^{current}_{Mol}$ (Section 2.2.1)
MAtom-init-2 kpc	$M_\odot$	M^{init}_{Atom} (Section 2.2.2)
PGrav	K cm^{-3}	P_{Grav}/k_B (Section 3.3)
PFeedback	K cm^{-3}	$P_{Feedback}/k_B$ (Section 3.3)
PDE	K cm^{-3}	$\langle P_{DE}\rangle/k_B$ from J. Sun et al. (2022, 2023) (Section 3.3)

Note. This table complements the nebular catalogs of B. Groves et al. (2023) and A. T. Barnes et al. 2025 with the basic H II region properties, masses, SFEs, and pressures needed to reproduce most figures. These catalogs can be joined using the RegionID from B. Groves et al. (2023). We request that users of these catalogs also cite the original measurements from B. Groves et al. (2023) and A. T. Barnes et al. 2025.

(This table is available in its entirety in machine-readable form in the online article.)

ORCID iDs

Debosmita Pathak https://orcid.org/0000-0003-2721-487X
Adam K. Leroy https://orcid.org/0000-0002-2545-1700
Ashley. T. Barnes https://orcid.org/0000-0003-0410-4504
Todd A. Thompson https://orcid.org/0000-0003-2377-9574
Laura A. Lopez https://orcid.org/0000-0002-1790-3148
Karin M. Sandstrom https://orcid.org/0000-0002-4378-8534
Jiayi Sun https://orcid.org/0000-0003-0378-4667
Simon C. O. Glover https://orcid.org/0000-0001-6708-1317
Ralf S. Klessen https://orcid.org/0000-0002-0560-3172
Eric W. Koch https://orcid.org/0000-0001-9605-780X
Kirsten L. Larson https://orcid.org/0000-0003-3917-6460
Janice Lee https://orcid.org/0000-0002-2278-9407
Sharon Meidt https://orcid.org/0000-0002-6118-4048
Patricia Sanchez-Blazquez https://orcid.org/0000-0003-0651-0098
Eva Schinnerer https://orcid.org/0000-0002-3933-7677
Zein Bazzi https://orcid.org/0009-0001-1221-0975
Francesco Belfiore https://orcid.org/0000-0002-2545-5752
Médéric Boquien https://orcid.org/0000-0003-0946-6176
Ryan Chown https://orcid.org/0000-0001-8241-7704
Dario Colombo https://orcid.org/0000-0001-6498-2945
Enrico Congiu https://orcid.org/0000-0002-8549-4083
Oleg V. Egorov https://orcid.org/0000-0002-4755-118X
Cosima Eibensteiner https://orcid.org/0000-0002-1185-2810
Sushma Kurapati https://orcid.org/0000-0001-6615-5492
Miguel Querejeta https://orcid.org/0000-0002-0472-1011
Daniel A. Dale https://orcid.org/0000-0002-5782-9093
Timo Kravtsov https://orcid.org/0000-0003-0955-9102
Mansi Padave https://orcid.org/0000-0002-3472-0490
D.J. Pisano https://orcid.org/0000-0001-7996-7860
Erik Rosolowsky https://orcid.org/0000-0002-5204-2259
Sumit K. Sarbadhicary https://orcid.org/0000-0002-4781-7291

Thomas G. Williams https://orcid.org/0000-0002-0012-2142
Remy Indebetouw https://orcid.org/0000-0002-4663-6827
Hsi-An Pan https://orcid.org/0000-0002-1370-6964
Leonardo Úbeda https://orcid.org/0000-0001-7130-2880
Amirnezam Amiri https://orcid.org/0000-0002-8553-1964
Frank Bigiel https://orcid.org/0000-0003-0166-9745
Guillermo A. Blanc https://orcid.org/0000-0003-4218-3944
Kathryn Grasha https://orcid.org/0000-0002-3247-5321

References

Astropy Collaboration, Price-Whelan, A. M., Sipőcz, B. M., et al. 2018, AJ, 156, 123
Astropy Collaboration, Robitaille, T. P., Tollerud, E. J., et al. 2013, A&A, 558, A33
Barnes, A. T., Chandar, R., Kreckel, K., et al. 2022, A&A, 662, L6
Barnes, A. T., Chandar, R., Kreckel, K., et al. 2025, arXiv:2510.11778
Barnes, A. T., Glover, S. C. O., Kreckel, K., et al. 2021, MNRAS, 508, 5362
Barnes, A. T., Longmore, S. N., Dale, J. E., et al. 2020, MNRAS, 498, 4906
Belfiore, F., Leroy, A. K., Sun, J., et al. 2023, A&A, 670, A67
Belfiore, F., Santoro, F., Groves, B., et al. 2022, A&A, 659, A26
Binder, B. A., & Povich, M. S. 2018, ApJ, 864, 136
Blackstone, I., & Thompson, T. A. 2023, MNRAS, 523, 4309
Bolatto, A. D., Wolfire, M., & Leroy, A. K. 2013, ARA&A, 51, 207
Chandar, R., Barnes, A. T., Thilker, D. A., et al. 2025, AJ, 169, 150
Chevance, M., Kruijssen, J. M. D., Hygate, A. P. S., et al. 2020, MNRAS, 493, 2872
Chevance, M., Krumholz, M. R., McLeod, A. F., et al. 2023, in ASP Conf. Ser., 534, Protostars and Planets VII, ed. S. Inutsuka et al. (San Francisco, CA: ASP), 1
Chiang, I.-D., Sandstrom, K. M., Chastenet, J., et al. 2024, ApJ, 964, 18
Chung, A., van Gorkom, J. H., Kenney, J. D. P., Crowl, H., & Vollmer, B. 2009, AJ, 138, 1741
Churchwell, E., & Goss, W. M. 1999, ApJ, 514, 188
Cosens, M., Wright, S. A., Murray, N., et al. 2022, ApJ, 929, 74
da Silva, R. L., Fumagalli, M., & Krumholz, M. 2012, ApJ, 745, 145
de Blok, W. J. G., Healy, J., Maccagni, F. M., et al. 2024, A&A, 688, A109
Della Bruna, L., Adamo, A., McLeod, A. F., et al. 2022, A&A, 666, A29
Di Cintio, A., Brook, C. B., Dutton, A. A., et al. 2014, MNRAS, 441, 2986
Dobbie, P. S., & Warren, S. J. 2020, OJAp, 3, 5
Egorov, O. V., Kreckel, K., Glover, S. C. O., et al. 2023, A&A, 678, A153
Eibensteiner, C., Sun, J., Bigiel, F., et al. 2024, A&A, 691, A163
Emsellem, E., Schinnerer, E., Santoro, F., et al. 2022, A&A, 659, A191
Fukushima, H., Yajima, H., Sugimura, K., et al. 2020, MNRAS, 497, 3830
Götberg, Y., de Mink, S. E., McQuinn, M., et al. 2020, A&A, 634, A134
Groves, B., Kreckel, K., Santoro, F., et al. 2023, MNRAS, 520, 4902
Grudić, M. Y., Guszejnov, D., Offner, S. S. R., et al. 2022, MNRAS, 512, 216
Grudić, M. Y., Hopkins, P. F., Quataert, E., & Murray, N. 2019, MNRAS, 483, 5548
Hannon, S., Lee, J. C., Whitmore, B. C., et al. 2022, MNRAS, 512, 1294
He, C.-C., Ricotti, M., & Geen, S. 2019, MNRAS, 489, 1880
He, C.-C., Ricotti, M., & Geen, S. 2020, MNRAS, 492, 4858
Howard, C. S., Pudritz, R. E., Harris, W. E., & Klessen, R. S. 2018, MNRAS, 475, 3121
Jiang, F., Benson, A., Hopkins, P. F., et al. 2023, MNRAS, 521, 4630
Jog, C. J. 2025, arXiv:2507.02062
Kennicutt, R. C., & Evans, N. J. 2012, ARA&A, 50, 531
Kim, J., Chevance, M., Kruijssen, J. M. D., et al. 2022, MNRAS, 516, 3006
Kim, J.-G., Kim, W.-T., & Ostriker, E. C. 2018, ApJ, 859, 68
Kim, J.-G., Kim, W.-T., & Ostriker, E. C. 2019, ApJ, 883, 102
Kim, J.-G., Ostriker, E. C., & Filippova, N. 2021, ApJ, 911, 128
Kimm, T., Bieri, R., Geen, S., et al. 2022, ApJS, 259, 21
Kreckel, K., Ho, I. T., Blanc, G. A., et al. 2019, ApJ, 887, 80
Kregel, M., van der Kruit, P. C., & de Grijs, R. 2002, MNRAS, 334, 646
Kroupa, P. 2001, MNRAS, 322, 231
Lada, C. J., & Lada, E. A. 2003, ARA&A, 41, 57
Lancaster, L., Kim, J.-G., Bryan, G. L., et al. 2025, ApJ, 989, 42
Lancaster, L., Ostriker, E. C., Kim, J.-G., & Kim, C.-G. 2021, ApJL, 922, L3
Lee, J. C., Sandstrom, K. M., Leroy, A. K., et al. 2023, ApJL, 944, L17
Leitherer, C., Ekström, S., Meynet, G., et al. 2014, ApJS, 212, 14
Leitherer, C., Schaerer, D., Goldader, J. D., et al. 1999, ApJS, 123, 3
Leroy, A. K., Sandstrom, K. M., Lang, D., et al. 2019, ApJS, 244, 24
Leroy, A. K., Schinnerer, E., Hughes, A., et al. 2021, ApJS, 257, 43
Leroy, A. K., Sun, J., Meidt, S., et al. 2025, ApJ, 985, 14
Levy, R. C., Bolatto, A. D., Leroy, A. K., et al. 2021, ApJ, 912, 4
Lopez, L. A., Krumholz, M. R., Bolatto, A. D., Prochaska, J. X., & Ramirez-Ruiz, E. 2011, ApJ, 731, 91
Lopez, L. A., Krumholz, M. R., Bolatto, A. D., et al. 2014, ApJ, 795, 121
Luridiana, V., Morisset, C., & Shaw, R. A. 2015, A&A, 573, A42
McKee, C. F., & Ostriker, E. C. 2007, ARA&A, 45, 565
McLeod, A. F., Ali, A. A., Chevance, M., et al. 2021, MNRAS, 508, 5425
Meidt, S. E., Glover, S. C. O., Klessen, R. S., et al. 2025, A&A, 700, A123
Meidt, S. E., Leroy, A. K., Querejeta, M., et al. 2021, ApJ, 913, 113
Menon, S. H., Burkhart, B., Somerville, R. S., Thompson, T. A., & Sternberg, A. 2025, ApJ, 987, 12
Menon, S. H., Federrath, C., & Krumholz, M. R. 2022, MNRAS, 517, 1313
Menon, S. H., Federrath, C., & Krumholz, M. R. 2023, MNRAS, 521, 5160
Mineo, S., Gilfanov, M., & Sunyaev, R. 2012, MNRAS, 426, 1870
Murray, N., Quataert, E., & Thompson, T. A. 2010, ApJ, 709, 191
Osterbrock, D. E., & Ferland, G. J. 2006, Astrophysics of Gaseous Nebulae and Active Galactic Nuclei (Mill Valley, CA: University Science Books)
Olivier, G. M., Lopez, L. A., Rosen, A. L., et al. 2021, ApJ, 908, 68
Ostriker, J. P., & McKee, C. F. 1988, RvMP, 60, 1
Pathak, D., Leroy, A. K., Thompson, T. A., et al. 2025, ApJ, 982, 140
Pedrini, A., Adamo, A., Calzetti, D., et al. 2024, ApJ, 971, 32
Querejeta, M., Leroy, A. K., Meidt, S. E., et al. 2024, A&A, 687, A293
Querejeta, M., Schinnerer, E., Meidt, S., et al. 2021, A&A, 656, A133
Rahner, D., Pellegrini, E. W., Glover, S. C. O., & Klessen, R. S. 2017, MNRAS, 470, 4453
Rahner, D., Pellegrini, E. W., Glover, S. C. O., & Klessen, R. S. 2019, MNRAS, 483, 2547
Randriamampandry, T. H., Wang, J., & Mogotsi, K. M. 2021, ApJ, 916, 26
Raskutti, S., Ostriker, E. C., & Skinner, M. A. 2016, ApJ, 829, 130
Relaño, M., Beckman, J. E., Zurita, A., Rozas, M., & Giammanco, C. 2005, A&A, 431, 235
Salo, H., Laurikainen, E., Laine, J., et al. 2015, ApJS, 219, 4
Santoro, F., Kreckel, K., Belfiore, F., et al. 2022, A&A, 658, A188
Scheuermann, F., Kreckel, K., Anand, G. S., et al. 2022, MNRAS, 511, 6087
Schinnerer, E., & Leroy, A. K. 2024, ARA&A, 62, 369
Storey, P. J., & Hummer, D. G. 1995, MNRAS, 272, 41
Sun, J., Leroy, A. K., Ostriker, E. C., et al. 2020, ApJ, 892, 148
Sun, J., Leroy, A. K., Ostriker, E. C., et al. 2023, ApJL, 945, L19
Sun, J., Leroy, A. K., Rosolowsky, E., et al. 2022, AJ, 164, 43
Sun, J., Leroy, A. K., Schruba, A., et al. 2018, ApJ, 860, 172
Thompson, T. A., & Krumholz, M. R. 2016, MNRAS, 455, 334
Topping, M. W., Sanders, R. L., Shapley, A. E., et al. 2025, MNRAS, 541, 1707
Vijayakumar, V., Sun, J., Ostriker, E. C., et al. 2025, ApJ, 989, 66
Walter, F., Brinks, E., de Blok, W. J. G., et al. 2008, AJ, 136, 2563
Watkins, E. J., Kreckel, K., Groves, B., et al. 2023, A&A, 676, A67
Williams, T. G., Lee, J. C., Larson, K. L., et al. 2024, ApJS, 273, 13
Zheng, Y., Wang, J., Irwin, J., et al. 2022, RAA, 22, 085004
Zhou, J. W., Kroupa, P., & Dib, S. 2025, MNRAS, 541, 1276